Pyrrolyl-silicon compounds with different alkyl spacer lengths: synthesis, electrochemical behavior and binding properties.

E. Volpi[a], L. Falciola[a], M. Trueba[a*], S.P. Trasatti[a], M.C. Sala[b], E. Pini[b], A. Contini[b]

[a]Dipartimento di Chimica, Università degli Studi di Milano, Via Golgi 19, 20133 , Milano, Italy

[b]Dipartimento di Scienze Farmaceutiche-Sezione Chimica Generale e Organica "A.Marchesini", Università degli Studi di Milano, Via Venezian 21, 20133 , Milano, Italy

*Corresponding author: monica.trueba@unimi.it

Abstract: This work reports a joint experimental-theoretical investigation of pyrrolyl-silicon compounds with different alkyl spacers, namely propyl, butyl and hexyl side chains carrying silicon-based end groups. For the electrochemical study, the monomers with methoxysilyl end groups spaced through butyl and hexyl chains were ad-hoc synthesized. Structurally different oligomeric domains are promoted during electropolymerization as a result of irreversible hydrolysis of methoxy end groups by acid intermediate σ-oligomers. The onset of OH-π stabilizing interactions and the charge pinning action of silanol promotes mixed n-p doping behavior of the hybrid films. The more important charge trapping in the case of propyl spacer is attributed to effective (through bond) inductive effects and conformational restrictions. MD simulations of chemisorption of hydrolyzed oligo-pyrroles onto γ-Al_2O_3 surface confirmed the propyl spacer as the optimum alkyl chain length for stratification and interpenetration of adsorbed hybrid layers.

Keywords: Pyrrolyl-silicon compounds, redox behavior, binding properties.

1. Introduction

Since the discovery of intrinsically conducting polymers (ICPs) in 1976 by MacDiarmid, Shirakawa and Heeger [1,2], research efforts have provided the basis for the development of new applications and new processing technologies [3-12]. A key aspect in the up growth of semiconducting ICP films with specific physico-chemical properties is the adhesion of the polymeric material to a given substrate (metallic, inorganic, bioinorganic). Bifunctional grafting with organosilanes by virtue of silanol groups coordination onto hydroxylated surfaces through hydrogen bonds constitutes a promising approach [13-15]. Since the pioneering work of Simon et al. [16], the integration of silane chemistry in the development of composite ICPs films have attracted increasing scientific interest in the field of solid state electronic devices [17-20] and biomedical applications [21-23].

N-substituted pyrrole and aniline with methoxysilylpropyl groups as precursors for direct-to-metal treatment of aluminum alloys have been extensively investigated by some of the co-authors [24-27]. The surface treatment with the corresponding hydrolysed solutions allowed to overcome the limited barrier protection against corrosion and the poor adhesion of contiguous polymeric films [28-30]. However, differently from the aniline derivative, the parent pyrrolyl-silicon compound (Fig. 1a, $\omega = 3$) presents peculiar properties such as the kinetic stabilization of silanol in solution and the n-type semiconducting behaviour of films deposited on FTO substrates. Theoretical studies indicated that intramolecular stabilization is determined by the donor-acceptor character of hydrolysed monomer and of oligomers linked α–α' via pyrrole rings, favouring non-covalent OH-π interactions between electron-deficient silanol group (Si-OH) and electron-rich pyrrole (Py) ring [31]. The charge-pinning action of Si-OH promoting Py ring saturation could explain the n-type semiconducting behaviour. Although these findings concur with the well-known

importance of the electronic properties of the substituents on the building up of ICPs networks [32], pyrrolyl-silicon structures seems to be promising for tailoring hybrid macromolecular networks with specific functions. Of concern is the influence of the length of the alkyl spacer on the physicochemical properties and molecular packing [33-37]. The special properties of Al and its alloys (low cost, light weight, high strength and surface reflectivity, among other) make them advantageous over other substrates [38], while damage by environmental corrosion is suppressed.

In this paper, the effect of the length of the alkyl chain spacer on the electrochemical behavior of N-[ω-(trimethoxysilyl)alkyl]-1H-pyrroles (Fig. 1a) and on the binding properties of hydrolyzed oligo-pyrrole structures (Fig. 1b) were investigated. For the electrochemical study, the monomers containing butyl and hexyl spacers (Fig. 1a, ω = 4,6) were ad-hoc synthesized and characterized by some of the co-authors with large experience in organic chemistry and structural elucidation [39-41]. The binding capabilities of hydrolyzed α–α' linked trimer structures (Fig. 1b) with hydroxylated ϒ-alumina (γ-Al_2O_3) surface were investigated by molecular dynamics (MD) by some of the co-authors with significant background on computational methods [42-44].

2. Experimental

2.1 Synthesis of N-[ω-(trimethoxysilyl)alkyl]-1H-pyrroles (ω = 4,6)

2.1.1 Materials and methods

All chemicals and anhydrous solvents were of reagent grade and used as supplied by Sigma-Aldrich, with the exception of dichloromethane CH_2Cl_2 which was distilled over CaH_2 under N_2

atmosphere before use. All the reactions were carried out under anhydrous inert conditions (N_2 atmosphere). All the glassware was dried in a heater over-night and cooled under vacuum.

Analytical TLC were carried out on pre-coated plates (silica gel 60, 250 µm layer thickness), using an UV lamp (254 nm) for visualization. Column chromatographies were performed with silica gel 60 (230-400 mesh). The ^{1}H and ^{13}C NMR spectra were taken on a Varian Mercury Plus 200, operating at 200 MHz for ^{1}H and 50.3 MHz for ^{13}C. Chemical shifts were expressed as ppm (δ) using the central peak of chloroform as internal reference (δ_H = 7.23 ppm; δ_C = 77.3 ppm). The APT sequence was used to distinguish methine and methylcarbon signals from those of methylene and quaternary carbons. FT-IR spectra were collected using the Spectrum One Perkin Elmer (MA, USA) FT-IR Spectrometer in the spectral region between 4000 and 600 or 450 cm^{-1} for solid or liquid compounds, respectively, and analyzed by transmittance technique with 32 scans and 4 cm^{-1} resolution. Solid samples were mixed in a mortar with KBr (1:100) and pressed in a hydraulic press (10 tons) into small tablets. For liquid samples one drop was placed between two plates of sodium chloride. Low resolution mass analyses were recorded with a Thermo-Finnigan LCQ advantage AP electro spray/ion trap equipped instrument by using a syringe pump device to directly inject sample solutions.

2.1.2 General synthetic procedures of pyrrolyl silicon compounds with butyl and hexyl spacers

N-[ω-(trimethoxysilyl)butyl]-1H-pyrrole and N-[ω-(trimethoxysilyl)hexyl]-1H-pyrrole (Fig. 1a, ω = 4,6) were synthesized following three steps, according to the general synthetic route in Scheme 1. The intermediate ω-alkenyl methanesulfonate (1a,b) and ω-alkenyl-1H-pyrrole (2a,b), and final N-[ω-(trimethoxysilyl)alkyl]-1H-pyrrole (3a,b) products were analyzed by ^{1}H and ^{13}C NMR, Mass

spectrometry, and FTIR (Supporting information, Table S1). Details of each synthesis step are given here below.

ω-alkenyl methanesulfonate (1a,b): To an ice-cold stirred solution of but-3-en-1-ol or hex-5-en-1-ol (5 g, 50 mmol) in dichloromethane (50 mL), triethylamine (10.52 mL, 75 mmol) and methanesulfonyl chloride (5.8 mL, 75 mmol) were added dropwise, and the mixture was stirred at 0°C for 1 h. A saturated aqueous NH_4Cl solution (50 mL) was added to the reaction and the mixture was extracted with Et_2O (2 x 100 mL). The combined organic layers were washed with water and brine and then dried over Na_2SO_4. The solvent was removed under reduced pressure (750mbar; 40°C; nitrogen atmosphere) to give a yellow oil of the corresponding mesylate.

ω-alkenyl-1H-pyrrole (2a,b): Under nitrogen atmosphere, pyrrole(2.66 mL, 483 mmol) was added to a stirred suspension of sodium hydroxide (3.86 g, 966 mmol) in dry DMSO (35.2 mL) at room temperature. After slow addition of a given methanesulfonate 1a-b (8.6 g, 483 mmol) at 0°C, the mixture was stirred during 14 h at room temperature. The reaction mixture was poured into ice water (75 mL) and extracted with Et_2O (3 x 100 mL). The combined organic layers were washed with water and brine, and then dried over Na_2SO_4. The solvent was removed under reduced pressure, and the residue was purified by column chromatography using EtOAc/hexane 2:98, to give the corresponding 1-(hex-5-enyl)-1H-pyrrole as a yellow oil.

N-[ω-(trimethoxysilyl)alkyl]-1H-pyrrole (3a,b): A mixture of ω-alkenyl-1H-pyrrole (6.39 g, 43 mmol) and a catalytic amount of hexachloroplatinic acid hexahydrate (0.72 mmol) was stirred during 30 min under nitrogen atmosphere. Trimethoxysilane (20.95 g, 172 mmol) was added dropwise, and the mixture was stirred during 6 hours at room temperature. Distillation under reduced pressure gives N-[ω-(trimethoxysilyl)alkyl]-1H-pyrrole as a yellow oil.

2.2 Electrochemical experiments

Electrochemical experiments were performed with a computer driven Autolab PGSTAT 12 potentiostat / galvanostat (EcoChemie, The Netherlands), using GPES 4.9 software. The electrochemical system consisted in a one compartment three-electrode glass cell with a capacity of 5 mL. The working electrode was a Pt disk with geometrical surface area of 0.7 cm^2 (Ø = 3 mm, AMEL). Pt wire and saturated calomel electrode (SCE) were used as counter and reference electrodes, respectively. Unless otherwise stated, potentials are reported throughout vs. SCE. The experiments were performed at room temperature under N_2 atmosphere.

The electrolyte solutions were prepared at a concentration of 0.1 M of tetrabutylammonium perchlorate TBAP (≥ 99.0%, Sigma Aldrich) in acetonitrile MeCN (≥ 99.8%, Sigma Aldrich). The synthesis solutions were prepared at a concentration of 4 mM of a given pyrrolyl-silicon monomer (Fig. 1a) in 0.1 M TBAP/MeCN. The N-substituted monomer with propyl spacer (98%, Sigma Aldrich) was used as received. Pyrrole (Aldrich) was studied in parallel for reference purposes. This monomer was distilled under argon atmosphere before use. The films were grown potentiodynamically by single-cycle potential scan and by recurrent potential cycling, using different anodic potential limits (E_A of +2.0, +1.4, +1.2 V). Translucent and brownish thin films were observed on the Pt surface at the end of the experiments. The redox behavior was evaluated by cyclic voltammetry using monomer-free 0.1 M TBAP/MeCN electrolyte. Unless otherwise indicated, the scan rate (ν) was 100 mV s^{-1}.

2.3 Molecular dynamic (MD) simulations

2.3.1 Construction of model hydroxylated γ-Al_2O_3 surface

Materials Studio 5.0 software was used for all calculations [45]. The model surface of hydroxylated γ-Al_2O_3 was constructed as described by Semoto et al. [46]. Briefly, the experimental coordinates of bulk γ-Al_2O_3 provided by Digne et al. [47] were used for the construction of the hydrated unit cell with 16 Al and 24 O atoms (a = 5.587 Å, b = 8.314 Å, c = 8.068 Å and β = 90.59°). Thereafter, the unit cell was sliced along the (0 0 1) plane and a 15 Å vacuum slab was added over the surface. The surface was solvated with a 10 Å layer of water molecules and then subjected to simulated annealing as follows: T = 300 K for 1 ps, 600 K for 1 ps and 300 K for 1 ps. Water chemisorption was simulated by ab-initio MD, following the protocol reported by Knaup and coworkers [48], and minimized using the CASTEP software package [49] (PBE functional [50], electron-ion interaction treated with ultrasoft pseudopotentials, plane-wave cutoff energy = 380 eV, all atoms except for the first and second layers frozen in their bulk positions). The final unit cell contained 52 atoms, corresponding to the original $Al_{16}O_{24}$ surface plus 4 chemisorbed H_2O molecules. The height of the cell was extended to 40 Å, a value well above the cutoff for non-bonded interactions (9.5 Å) to prevent the adsorbate from seeing the bottom of the cell imaged along the z axis in periodic boundary condition (PBC) calculations. The resulting cell unit was fused together to obtain supercells with different sizes (2x1x1, 2x2x1, 3x1x1, 3x2x1, 3x3x1, 4x1x1 and 4x2x1) and thereafter optimized by MD simulations (Discover, 100 ps, T = 300 K, NVT ensemble and Nosè –Hoover thermostat, COMPASS force field [51]) of the adsorption of four hydrolyzed monomer units with ω = 3 (Fig. 1b) with the help of the *Adsorption Locator*. The trajectory analysis indicated the 3x2x1 supercell (a = 16.8 Å, b = 16.6 Å, c = 40.0 Å, β = 90.6°) as the most suited, allowing enough space to load the organosilanes without affecting excessively the computation time.

2.3.2 Adsorption of hydrolyzed α–α' linked Py oligomers

Trimer structures of α–α' Py linked and fully-hydrolyzed monomers (Fig.1b) were used as model compounds for MD simulation of chemisorption on the hydroxilated γ-Al_2O_3 model supercell surface. Trimer conformations were generated by a stochastic conformational search performed by using the Boltzmann Jump method of the *Conformer* module. The *Adsorption Locator* module, operating through the configurational bias method, was used for protocol evaluation, using different SA cycles (15, 30, 60) and number of production steps (10^6, 20^6 and 40^6). The maximum number of loading steps was kept constant at 10^6 and the final temperature was set to 0 K. After optimization of the six lowest energy docked structures of each set of trimer molecules by using the *Forcite* module (COMPASS forcefield, quality = fine), the minima energy conformer for a given model trimer was solvated with MeOH and H_2O molecules in a proportion 90:10 to simulate the experimental hydroalcoholic solvent mixture [29] and subjected to MD simulations (*Discovery*, COMPASS force field, NVT, T = 300 K, Nosè-Hoover thermostat, time step 1.0 fs, 100 ps of solvent equilibration, 1 ns of simulation time, unless otherwise indicated), using positional constraints on the surface atoms. Interaction energies were calculated on the last 500 ps of the MD trajectory, following the method reported by Kornherr *et al*. [52].

3. Results and discussion

3.1. Synthesis and spectroscopic characterization of pyrrolyl-silicon monomers with butyl and hexyl spacers

The procedure reported in the literature for the synthesis of N-[6-(trimethoxysilyl)hexyl]-1H-pyrrole (Fig. 1a) comprises four steps [53]. Briefly, the alkylation of pyrrole with 1-bromo-5-

hexene, obtained by dehydrobromination of 1,6-dibromohexane, followed by silylation of the double bond using trimethoxysilane in the presence of hexachloroplatinic acid as the catalyst. This synthetic route was modified as depicted in Scheme 1 in order to reduce the synthesis steps, to increase the reaction yields and to simplify the purification procedures. That is, commercially available ω-alkenyl alcohol was converted into the corresponding mesylate, which is a better leaving group for the successive step of sodium pyrrole anion N-alkylation. Finally, double bond silylation in the presence of catalytic amounts of hexachloroplatinic acid allowed to obtain the pyrrolyl silicon compounds with butyl and hexyl spacers (Fig. 1a). The general reaction route in Scheme 1 provided good yield of intermediates and final products (Table S1).

According to the spectroscopic characterization results (Table S1), NMR analyses confirmed the structure of all intermediate and final compounds. The full mass spectra showed molecular ion peaks conforming to calculated molecular weights. The FTIR spectra of ω-alkenyl-1H-pyrroles (2a-b, Scheme 1) showed the characteristic bands for pyrrole Csp^2-H stretching at 3100 and 3076 cm^{-1}, the typical aromatic C=C stretching in plane vibration of the pyrrole ring in the range between 1500 and 1357 cm^{-1} and the C-N ring strong stretching at 1283 cm^{-1}, being diagnostic for 1-alkyl pyrroles. In addition the spectra evidenced the Csp^3-H stretching at 2942-2841 cm^{-1}, the C=C olefinic stretching at 1640 cm^{-1} and the rocking bands of CH_2 at 723 cm^{-1}. The silylation of the alkenyl double bond giving the N-[ω-(trimethoxysilyl)alkyl]-1H-pyrroles (3a-b, Scheme 1) was indicated by the characteristic stretching vibrations of Si-OCH_3 and of Si-O at 1191 and 1087 cm^{-1}, respectively, and by the absence of C=C olefinic stretching (1640 cm^{-1}). The differences above are shown in Figure 2 for the compounds with hexyl spacer (2b and 3b, Scheme 1).

The synthetic route proposed herein (Scheme 1) allowed to obtain the desired compounds with good yield and purity, thus constituting an efficient alternative for the synthesis of N-[ω-(trimethoxysilyl)alkyl]-1H-pyrroles.

3.2 Electropolymerization and solid state processes

Figure 3 shows the single-cycle voltammograms recorded during the electropolymerization of pyrrole and of pyrrolyl-silicon monomers (Fig. 1a) using an anodic potential limit E_A of +2.0 V and different scan rates (ν between 10 mV s^{-1} – 200 mV s^{-1}). The detection of anodic peaks at about +1.25 V and +1.55 V for all the monomers indicates that the donor character of Py ring is preserved with N-alkylsilylmethoxy substitution, as predicted by theory [31] and reported for other N-substituted pyrroles [34]. The intensity of the anodic peaks is comparable in the case of pyrrole monomer (Fig. 3a), regardless the scan rate. Conversely, for N-substituted monomers, the first anodic peak is more intense unless the stay time at more positive potentials is raised by decreasing ν (≤ 20 mV s^{-1}), thus promoting crosslinking of accessible redox sites. In addition, the intensity of both peaks depends non-monotonically on the length of the alkyl spacer, decreasing in the order (Fig. 3b-c): propyl (ω = 3) > hexyl (ω = 6) > butyl (ω = 4), regardless the scan rate. The shift of both peaks to higher potential values by increasing ν also differs from the case of pyrrole monomer, resulting more evident in the case of the N-substituted monomer with propyl spacer (ω = 3). Logarithmic plots of the current of the first anodic peak as a function of ν gave linear relationships with slopes of about 0.5 in the case of pyrrolyl-silicon monomers, indicating diffusion-limited nucleation and growth of hybrid oligomers due to steric effects. Ppy and the

hybrid films showed poor electroactivity in monomer-free 0.1 TBAP/MeCN and the associated redox peaks (E < +1.0 V) decreased markedly with cycling.

Pyrrole gives small oligomers when no water is intentionally added to acetonitrile solutions due to disfavored proton elimination of σ-oligomers [4]. Thus, the anodic features of PPy (Fig. 3a) are ascribed to the electrodeposition of small σ-oligomers and crosslinking reactions through interchain σ-couplings, respectively, the latter leading to conjugation disruption and limited charge transport. In the case of hybrid monomers, steric effects disfavor the electrodeposition of the hybrid films while restrain crosslinking reactions by shielding of accessible redox states. Concerning the effect of the alkyl side chain, effective inductive (through bond) effects [35] are likely more significant in the case of N-substituted monomer with propyl side chain (ω = 3) (Fig. 3b). The privileged electrogrowth of the hybrid film with flexible hexyl chain (ω = 6) in comparison with that with butyl spacer (ω = 4) (Fig. 3c,d) is indicative of cumulative electronic effects and minor contribution of steric shielding.

The trend of the first anodic peak with N-substitution and with the length of the alkyl spacer is reproduced by carrying out the single-cycle electropolymerization using smaller E_A = +1.4 V (ν = 100 mV s^{-1}) (Fig. 4). The distinct crossing between the forward and reverse curves in the case of Py manifests comproportionation reactions between intermediate σ-oligomers and monomers [4]. This autocatalytic mechanism aiding monomer oxidation is restrained with N-substitution due to steric hindrance. The voltammograms recorded during films growth by recurrent potential cycling are reported in Figure 5. The voltammetric behavior of PPy (Fig. 5a) reproduces reported data rather well [4]. The increase with cycling of the oxidation peak at +1.3 V and of the broad redox waves between -0.2 and +1.0 V corresponds to the growth of a polydisperse polymer film as a result of increasing available redox states and their superposition as the chain length increases.

Conversely, in the case of N-substituted monomers, a sharp oxidation peak at about +1.2 V is detected during the first anodic scan (Fig. 5b-d). This peak decreases markedly in the following cycle and subsequently evolves to a more positive growing peak. The redox response of the hybrid films are detected at more positive potentials in comparison with that of PPy. Nonetheless, the corresponding oxidation and reduction waves are comprised in a narrower and similar potential range (between +0.2 and +1.0 V). In addition, the redox oxidation wave splits into two bands at about +0.4 and 0.9 V after few cycles that progressively merge to give a single in-between anodic feature. The intensity, shape and broadness of the reduction wave changes less markedly with recurrent cycling.

The results above point to a fast radical coupling of the pyrrolyl-silicon monomers to form α–α' dimers or small oligomers, but disfavored growth of the hybrid films via subsequent coupling steps. Thus, less conjugated structures develop with consecutive cycling due to geometrically constrained coupling reactions and proton elimination of bulky σ-oligomers, also involving confined solid state processes as manifested by the well-defined isopotential anodic points at about +1.0 V (Fig. 5b-d). Higher geometrical distortion of oligomeric conformations is likely for the case of the butyl side chain (Fig. 5c). The electroactivity of the corresponding films in monomer-free electrolyte solutions decreased markedly with cycling (Fig. S1). Nonetheless, the reduction band was always less intense than the corresponding oxidation wave. Only in the case of N-substituted monomer with propyl spacer (ω = 3), two anodic features were still identified, while the weak reduction peak at about 0.0 V, ascribable to proton discharge of σ-oligomers [4], was hardly distinguished. Although this conforms to the expected decrease of σ-oligomers reactivity as the polymeric chain increases, the remaining two anodic features suggests formation of structurally different oligomeric species.

The above observation is further indicated by the voltammetric responses recorded during simultaneous polymerization using smaller anodic potential limit (E_A = +1.2 V) (Fig. 6). While the redox features of PPy change little (Fig. 6a), the charging/discharging of the hybrid films at E > + 0.1 V is featured by two well defined anodic redox peaks and a prevalent reduction wave (Fig. 6b-c), regardless the length of the alkyl side chain. Several redox bands at more negative potentials are detected for the case of the butyl spacer only (Fig. 6c). However, these disappear with recurrent cycling, thus ascribable to unstable oligomeric species. The importance of the anodic features at about +0.4 and +0.9 V decreases with the length of the alkyl spacer as indicated before, *i.e.* propyl (ω = 3) > hexyl (ω = 6) > butyl (ω = 4), but their intensity tend to become equivalent with cycling in the case of the former spacer (Fig. 6b). In addition, the discharge of protons of σ-oligomers at about 0.0 V is indistinguishable. This feature increases with cycling in the case of the butyl spacer only (Fig. 6c). The electroactive behavior of the hybrid films in monomer-free electrolyte is dominated by charge transport processes at E > + 0.1 V (Fig. 7). Reduction peaks typical of proton discharge of σ-oligomers (around 0.0 V) are hardly detected, while several isopotential points are well discerned, being indicative of formation of new electroactive species without side reactions.

Overall results indicate that proton discharge is limited with the decreasing E_A, and thus with the increase of σ-oligomers reactivity as the PPy oligomeric chain length decreases [4]. The apparent stability of these intermediate species while the two anodic features become important (Figs. 5 and 6) suggests participation of the free protons of intermediate oligomers in the film growth and solid state processes. Structurally different oligomeric domains, more likely hydrolyzed and non-hydrolyzed structures, could be formed due to irreversible changes associated to chemical reactions between reactive methoxy groups and confined “free” protons. The

irreversible anodic peak at about +0.4 V is thus ascribed to hydrolyzed structures with donor-acceptor character and stabilized by noncovalent interactions between silanol end group and the π system of pyrrole ring [31]. The incomplete discharging of the hydrolyzed oligomeric domains due to the charge pinning action of the electron-deficient silanol group requires charge compensation by electrolyte cations that diffuse back to the solution during the anodic scan. As for PPy, peaks ascribable to hybrid films reduction were not detected by using very negative potential limits up to -2.5 V. The more important charge trapping indicated for the case of the propyl side chain with effective inductive (through bond) effects but higher conformational restriction points to heterogeneous kinetics governing the irreversible structural changes of the hybrid films. It is to be noticed that the redox features of PPy [4] and of poly(N-methyl pyrrole) [54] are reported to be closely similar, whereas two anodic though ill-defined bands have been detected for N-hydroxyhexyl pyrrole as starting monomer under similar test conditions over a number of different N-substituted pyrrole derivatives [34].

Present findings are in accordance with the n-type semiconducting behavior of films deposited on FTO substrates using hydrolyzed solutions of N-[3-(trimethoxysilyl)propyl]-1H-pyrrole (unpublished results) [31]. The prevalent n-type charge transport contributes to the outstanding protection of the as-deposited thin (2 – 5 μm) hybrid films against corrosion of aluminum alloys in chloride containing solutions. Although longer alkyl side chains should inhibit the back-hydrolysis of siloxane bonds, the instauration of OH-π interactions is less favored, thus affecting the semiconducting behavior and the protection capability.

3.3. Binding properties of hydrolyzed pyrrolyl-silicon oligomers on hydroxylated ϒ-Al_2O_3

Surface treatment with organosilanes exploit the special chemistry of silanol to react with OH-rich substrates (glass, minerals and metals) through simple and feasible chemical steps (adsorption and condensation) [13]. The electrodeposition of PPy on reactive metals like Al alloys requires more complicated activation steps [24,28], whereas attempts to electrodeposit hybrid films using neat and hydrolyzed pyrrolyl-silicon monomers were unsuccessful. Correspondingly, the effect of the alkyl spacer length on the binding properties of hydrolyzed N-substituted oligo-pyrroles was theoretically investigated. Based on previous experimental and theoretical results, fully hydrolyzed trimer structures linked α–α' via Py ring (Fig. 1b) were chosen for MD simulations of interactions with hydroxylated ϒ-Al_2O_3 model surface.

Geometrical descriptors of the trimer/ ϒ-Al_2O_3 complexes, namely the average H-bond distances between silanol and hydroxyl atoms of the surface and the average inter-ring NCCN rotational angle (θ) between adjacent α–α' linked pyrrole rings, were estimated from the MD trajectories of six different binding conformations for given trimer structures (ωC1 – ωC6, ω = 3, 4 and 6). The interaction energies between a given trimer structure and the hydroxylated surface were computed by the method proposed by Kornherr *et al.* [52] for organosilanes bounded to a ZnO surface, using the following equation:

$$\Delta E_{interact} = E_{surf+silane} - [E_{surf} + E_{silane}] \qquad (1)$$

where $\Delta E_{\text{interact}}$ represents the total potential energy of the interacting interface $E_{surf\,+\,silane}$ counterbalanced by the total potential energy of each component of the interface E_{surf} and E_{silane}

The results for most stable binding conformers are reported in Table 1. For each interacting –$Si(OH)_3$ group, the number of H-bonds matching requested thresholds (average donor-H-acceptor angle > 120°, average H···acceptor distance < 2.2 Å) was between 1 and 8. Details of the H-bond distribution are provided as supporting information (Figs. S2-S4).

The analysis of the interaction energies points out two energetically equivalent trimer conformers for trimer structures with propyl spacer, namely 3C2 and 3C3 (Fig. 8a,b). These present an appreciable number of H bonds (11 and 14, respectively), and inter-ring torsion angles (θ_1 and θ_2) that correspond to an *anti* periplanar conformation (Table 1). Nonetheless, the interaction modes consistently differ. The conformer 3C2 (Fig. 8a) binds the surface through two silanol end groups of adjacent side chains, while the third end group is fully solvated (solvent molecules not shown) and points toward the top of the cell, i.e. along the z axis. Conversely, the conformer 3C3 (Fig. 8b) binds the surface through the hydroxysilyl groups of terminal pyrrole rings, standing up (z axis) the end group of the central Py ring. In addition, the oligo-pyrrole chain of 3C2 tilts by an angle of about 30° with respect to the surface plane, whereas the α–α' linked Py rings lie almost parallel to the surface in the case of 3C3. Only one interacting hydroxysilyl group was obtained for the conformer 3C1 (Figs. S5 and S6).

The binding capability decreases with the length of the alkyl side chain. Among the trimer conformers with butyl spacer (ω = 4), only 4C3 presents a strong interaction energy, the most negative in comparison to the other binding conformers (Table 1). The number of H-bonds is comparable to that of 3C3, but the binding mode involves the silanol groups of all the three side chains (Fig. 8c). The propensity to form oligomer/surface complexes is smaller for the other two stable conformers 4C1 and 4C2 (Table 1), in spite of binding modes similar to those of 3C3 and 3C2, respectively (Fig. S7). Only the 4C1 conformer presents θ_1 and θ_2 values that correspond to a

syn periplanar conformation of oligo-pyrrole chain. The H bond capability decreases further for trimer structures with hexyl spacer (6C1 – 6C3, Table 1). Among these, only the conformer 6C3 presents a relatively high negative interaction energy and the corresponding oligomer/surface complex resembles closely that of 3C2 (Fig. 8a,d), presenting similar torsion angles as well (≈ 180°, Table 1), though the number of possible H bonds is 6. Less interacting are the binding conformers 6C2 and 6C1 (Fig. S8).

Summing up MD simulations results, the H-bonding of hydrolyzed trimer structures through silanol chemisorption onto hydroxylated γ-Al_2O_3 surface decreases with the length of the alkyl side chain due to higher conformational freedom. The binding mode appears to play a less important role. Considering that the stratification of oligomeric structures is expected to be enhanced through both pyrrole ring linking and silanol condensation, higher macromolecular order is predicted for the oligomeric structures with propyl side chain (Fig. 8a,b). The preferred up-down arrangement of the hydrolyzed side chains is expected to favor also intermolecular OH-π stabilizing interactions within the adsorbed hybrid network. If the surface coverage with silanol groups is significant such as to force the oligo-pyrrole chain parallel to the surface, as predicted for conformers with butyl spacer (Fig. 8b), the stratification and stabilizing interactions are disfavored. The higher flexibility of conformers with hexyl side chains allows for binding modes that are compatible with stratification, though to a lesser extent. Recall of electrochemical results, both fundamentally different approaches converge to indicate that the buildup of interpenetrating hybrid network entanglement is privileged in the case of N-substituted monomer with propyl side chain.

4. Conclusions

Pyrrolyl-silicon compounds with variable spacing between pyrrole and silicon-based end groups through propyl, butyl and hexyl chains, were investigated by cyclic voltammetry and MD simulations. The N-substituted monomers with butyl and hexyl side chains were ad-hoc designed and successfully synthesized for the electrochemical study. The electrochemical buildup of the hybrid network is driven by conformation-controlled heterogeneous kinetics involving irreversible chemical reactions, namely acid-catalyzed hydrolysis of methoxy groups by the free protons of σ-oligomers. The donor-acceptor character of the irreversible hydrolyzed structures enhances the stability through OH-π stabilizing interactions and promote mixed n-p charge transport due to the charge pinning action of silanol. The hybrid monomer with propyl spacer is more prone to form interpenetrated macromolecular domains of hydrolyzed and non-hydrolyzed oligomers as a result of effective (through bond) inductive effects and conformational restrictions. MD simulations predict that the binding capacity of hydrolyzed N-substituted oligo-pyrroles onto γ-Al_2O_3 surface is conformationally controlled as well. The stratification of oligomers endowed with propyl side chain is also privileged in the presence of a reactive surface. The two fundamentally different approaches converge to indicate the propyl spacer as the optimum side chain for OH-π stabilizing interactions.

Acknowledgements

This work was carried out in the framework of the project “Corrosion protection of light alloys by conducting polymers and silane-based coatings” supported by Fondazione Cariplo, grant n° 2010:0458.

References

[1] H. Shirakawa, E.J. Louis, A.G. MacDiarmid, C.K. Chiang, A. Heeger, Synthesis of electrically conducting organic polymers: halogen derivatives of polyacetylene, (CH)x, J. Chem. Soc., Chem. Commun. (1977) 578 – 580.

[2] C.K. Chiang, C.R. Fincher, Jr., Y.W. Park, A.J. Heeger, H. Shirakawa, E.J. Louis, S.C. Gau, and Alan G. MacDiarmid, Electrical conductivity in doped polyacetylene, J Phys. Rev. Lett. 39 (1977) 1098 – 1101.

[3] A.J. Heeger, Semiconducting and metallic polymers: The fourth generation of polymeric materials, J. Phys. Chem. B 105 (2001) 8475 – 8491.

[4] J. Heinze, B.A. Frontana-Uribe, S. Ludwigs, Electrochemistry of conducting polymers - persistent models and new concepts, Chem. Rev. 110 (2010) 4724 – 4771.

[5] T.F. Otero, J.G. Martinez, J. Arias-Pardilla, Biomimetic electrochemistry from conducting polymers. A review. Artificial muscles, smart membranes, smart drug delivery and computer/neuron interfaces, Electrochim. Acta 84 (2012) 112 – 128.

[6] G. Yua , X. Xie, L. Pan, Z. Bao, Y. Cui, Hybrid nanostructured materials for high-performance electrochemical capacitors, Nano Energy 2 (2013) 213 – 234.

[7] U. Riaz, C. Nwaoh, S.M. Ashraf, Recent advances in corrosion protective composite coatings based on conducting polymers and natural resource derived polymers, Prog. Org. Coat. 77 (2014) 743 – 756.

[8] D.T. Simon, E.O. Gabrielsson, K. Tybrandt, M. Berggren, Organic bioelectronics: Bridging the signaling gap between biology and technology, Chem. Rev. 116 (2016) 13009 − 13041.

[9] A.M. Bryan, L.M. Santino, Y. Lu, S. Acharya, J.M. D'Arcy, Conducting polymers for pseudocapacitive energy storage, Chem. Mater. 28 (2016) 5989 − 5998.

[10] S. Shrivastava, N. Jadon, R. Jain, Next-generation polymer nanocomposite-based electrochemical sensors and biosensors: A review, Tr. Anal. Chem. 82 (2016) 55 – 67.

[11] A. Mirabedini, J. Foroughi, G.G. Wallace, Developments in conducting polymer fibres: from established spinning methods toward advanced applications, RSC Adv. 6 (2016) 44687 – 44716.

[12] S. Ahn, S-H. Jeong, T-H. Han, T-W. Lee, Conducting polymers as anode buffer materials in organic and perovskite optoelectronics, Adv. Optical Mater. 5 (2017) 16005121 – 16005124.

[13] E.P. Plueddeman, Silane Coupling Agents, Second ed., Plenum Press, New York, 1990.

[14] M. Ammar, C. Smadja, G. Thi Phuong Ly, D. Tandjigora, J. Vigneron, A. Etcheberry, M. Taverna, E. Dufour-Gergam, Chemical engineering of self-assembled Alzheimer's peptide on a silanized silicon surface, Langmuir 30 (2014) 5863 − 5872.

[15] T. Mondal, A.K. Bhowmick, R. Krishnamoorti, Conducting instant adhesives by grafting of silane polymer onto expanded graphite, ACS Appl. Mater. Interfaces 6 (2014) 16097 − 16105.

[16] R.A. Simon, A.J. Ricco, M.S. Wrighton, Synthesis and characterization of a new surface derivatizing reagent to promote the adhesion of polypyrrole films to N-type silicon photoanodes: N-(3-(trimethoxysilyl)propyl)pyrrole, J. Am. Chem. Soc. 104 (1982) 2031 – 2034.

[17] E. Jaehne, S. Oberoi, H. Adler, Ultra-thin layers as new concepts for corrosion inhibition and adhesion promotion, Prog. Org. Coat. 61 (2008) 211 – 223.

[18] L. Valentini, M. Cardinali, J.M. Kenny, Selective deposition of semiconducting single-walled carbon nanotubes onto amino-silane modified indium tin-oxide surface for the development of poly(3-hexylthiophene)/ carbon-nanotube photovoltaic heterojunctions, Carbon 48 (2010) 861 – 867.

[19] H. Wang, V. Kumara, Transparent and conductive polysiloxanes/PEDOT:PSS nanocomposite thin films with a "water-impermeable" property to significantly enhance stability of organic–inorganic hybrid solar cells, RSC Adv. 5 (2015) 9650 – 9657.

[20] S. Kim, A. Cho, S. Kim, W. Cho, M.H. Chung, F.S. Kim, J.H. Kim, Multi-purpose overcoating layers based on PVA/silane hybrid composites for highly transparent, flexible, and durable AgNW/PEDOT:PSS films, RSC Adv. 6 (2016) 19280 – 19287.

[21] A. Kros, J.A. Jansen, S.J. Holder, R.J.M. Nolte, N.A.J.M. Sommerdijk, Silane-based hybrids for biomedical applications, J. Adh. Sci. Technol. 16 (2002) 143 – 155.

[22] U.G. Spizzirri, M. Curcio, G. Cirillo, T. Spataro, O. Vittorio, N. Picci, S. Hampel, F. Iemma, F.P. Nicoletta, Recent advances in the synthesis and biomedical applications of nanocomposite hydrogels, Pharmaceutics 7 (2015) 413 – 437.

[23] M. Karakoy, E. Gultepe, S. Pandey, M.A. Khashab, D.H. Gracias, Silane surface modification for improved bioadhesion of esophageal stents, Appl. Surf. Sci. 311 (2014) 684 – 689.

[24] (a) M. Trueba, S.P. Trasatti, Pyrrole-based silane primer for corrosion protection of commercial Al alloys. Part I: Synthesis and spectroscopic characterization. Prog. Org. Coat. 66 (2009) 254 − 264; (b) *ibid.*, Part II. Corrosion Performance in Neutral NaCl Solution, *ibid.*, 265−275.

[25] D.O. Flamini, M. Trueba, S.P. Trasatti, Aniline-based silane as a primer for corrosion inhibition of aluminium, Prog. Org. Coat. 74 (2012) 302 − 310.

[26] M. Trueba, S.P. Trasatti, D.O. Flamini, The effect of aluminium alloy secondary phases on aniline-based silane protection capacity, Corros. Sci. 63 (2012) 59 − 70.

[27] S. Bianchi, M. Trueba, S.P. Trasatti, E. Madaschi, M.C. Sala, An in-depth comprehension of the protection mechanism of Al alloys by aniline-based silane, Prog. Org. Coat. 77 (2014) 2054 − 2065.

[28] M. Rizzi, M. Trueba, S.P. Trasatti, Polypyrrole films on Al alloys: The role of structural changes on protection performance, Synth. Met. 161 (2011) 23 – 31.

[29] E. Volpi, M. Trueba, S.P. Trasatti, Electrochemical investigation of conformational rearrangements of polypyrrole deposited on Al alloys, Prog. Org. Coat. 74 (2012) 376 – 384.

[30] E. Volpi, M. Trueba, S.P. Trasatti, S. Trasatti, Effect of polypyrrole conformational rearrangement on Al alloys corrosion protection, J. Electroanal. Chem 688 (2013) 289 – 297.

[31] S. González-Santana, C. Morera-Boado, L.A. Montero-Cabrera, M. Trueba, S.P. Trasatti, Pyrrolyl−silicon compounds as precursors for donor−acceptor systems stabilized by noncovalent interactions, J. Phys. Chem. A 119 (2015) 7038 − 7051.

[32] R. J. Waltman, J. Bargon, Electrically conducting polymers: a review of the electropolymerization reaction, of the effects of chemical structure on polymer film properties, and of applications towards technology, Can. J. Chem. 64 (1986) 76 – 95.

[33] M.J.J. Hetem, J.J.W. de Haan, H.A. Claessens, L.J.M. van de Ven, C.A. Cramers, Influence of alkyl chain length on the stability of n -alkyl-modified reversed phases. 2. Model dissolution study, Anal. Chem. 62 (1990) 2296 – 2300.

[34] Z. Deng, D.C. Stone, M. Thompson, Characterization of polymer films of pyrrole derivatives for chemical sensing by cyclic voltammetry, X-ray photoelectron spectroscopy and vapour sorption studies, Analyst 122 (1997) 1129 – 1138.

[35] R. Tandon, T.A. Nigst, H. Zipse, Inductive effects through alkyl groups – How long is long enough? Eur. J. Org. Chem. (2013) 5423 – 5430.

[36] H. Yu, K.H. Park, I. Song, M.-J. Kim, Y.-H. Kim, J.H. Oh, Effect of the alkyl spacer length on the electrical performance of diketopyrrolopyrrole-thiophene vinylene thiophene polymer semiconductors, J. Mater. Chem. C 3 (2015) 11697 – 11704.

[37] S. Ogi, V. Stepanenko, J. Thein, F. Würthner, Impact of alkyl spacer length on aggregation pathways in kinetically controlled supramolecular polymerization, J. Am. Chem. Soc. 138 (2016) 670 − 678.

[38] K. Saranya, M. Rameez, A. Subramania, Developments in conducting polymer based counter electrodes for dye-sensitized solar cells – An overview, Eur. Pol. J. 66 (2015) 207 – 227.

[39] N. Basilico, M. Migotto, D. Patoinewende Ilboudo, D. Taramelli, R. Stradi, E. Pini, Modified quaternary ammonium salts as potential antimalarial agents, Bioorg. Med. Chem. 23 (2015) 4681 – 4687.

[40] N. Ferri, G. Facchetti, S. Pellegrino, C. Ricci, G. Curigliano, E. Pini, I. Rimoldi, Antiproliferative platinum(II) complexes based on imidazole moiety: synthesis, evaluation in HCT-116 cancer cell line and interaction with Ctr-1 Met-rich domain, Bioorg. Med. Chem. 23 (2015) 2538 – 2547.

[41] A. Ionescu, R. Lento, T.F. Mastropietro, I. Aiello, R. Termine, A. Golemme, M. Ghedini, N. Bellec, E. Pini, I. Rimoldi, N. Godbert, Electropolymerized highly photoconductive thin films of cyclopalladated and cycloplatinated complexes, ACS Appl. Mater. Interfaces 7 (2015) 4019 – 4028.

[42] I. Maffucci, A. Contini, Improved computation of protein–protein relative binding energies with the Nwat-MMGBSA method, J. Chem. Inf. Model. 56 (2016) 1692 – 1704.

[43] I. Maffucci, A. Contini, An updated test of AMBER force fields and implicit solvent models in predicting the secondary structure of helical, β-Hairpin, and intrinsically disordered peptides" J. Chem. Theory Comput. 12 (2016) 714 – 727.

[44] I. Maffucci, A. Contini, Explicit ligand hydration shells improve the correlation between MM-PB/GBSA binding energies and experimental activities, J. Chem. Theory Comput. 9 (2013) 2706 – 2717.

[45] Accelrys Materials Studio 5.0, Vol. Accelrys Software, Inc., San Diego, CA, 2010.

[46] T. Semoto, Y. Tsuji, K. Yoshizawa, Molecular understanding of the adhesive force between a metal oxide surface and an epoxy resin, J. Phys. Chem. C 115 (2011) 11701 – 11708.

[47] M. Digne, P. Sautet, P. Raybaud, P. Euzen, H. Toulhoat, Hydroxyl groups on γ-alumina surfaces: A DFT study, J. Catalysis 211 (2002) 1 – 5.

[48] J. M. Knaup, C. Köhler, T. Frauenheim, A.T. Blumenau, M. Amkreutz, P. Schiffels, B. Schneider, O.-D. Hennemann, Computational studies on polymer adhesion at the surface of γ-Al2O3: I. The adsorption of adhesive component molecules from the gas phase, J. Phys. Chem. B 110 (2006) 20460 – 20468.

[49] S.J. Clark, M.D. Segall, C.J. Pickard, P.J. Hasnip, M.J. Probert, K. Refson, M.C. Payne, First principles methods using CASTEP, Z. Kristallogr. 220 (2005) 567 – 570.

[50] J.P. Perdew, K. Burke and M. Ernzerhof, Generalized gradient approximation made simple, Phys. Rev. Lett. 77 (1996) 3865 – 3868.

[51] H. Sun, COMPASS: An ab Initio Force-field optimized for condensed-phase applications. Overview with details on alkane and benzene compounds, J. Phys. Chem. B 102 (1998) 7338 – 7364.

[52] (a) A. Kornherr, S.A. French, A.A. Sokol, C.R.A. Catlow, S. Hansal, W.E.G. Hansal, J.O. Besenhard, H. Kronberger, G.E. Nauer, G. Zifferer, Interaction of adsorbed organosilanes with polar zinc oxide surfaces: a molecular dynamics study comparing two models for the metal oxide surface, Chem. Phys. Lett. 393 (2004) 107 – 111; (b) A. Kornherr, S. Hansal, W.E.G. Hansal, J.O. Besenhard, H. Kronberger, G.E. Nauer, G. Zifferer, Molecular dynamics simulations of the adsorption of industrial relevant silane molecules at a zinc oxide surface, J. Chem. Phys. 119 (2003) 9719 – 9728.

[53] S. Kato, F.-Q. Chen, C. Pac, Anchoring effects of self-assembled monolayers for polymer-dispersed liquid crystal films, J. Phys. Chem. B 108 (2004) 320 – 326.

[54] A. Cambra, M.I. Redondo, M.J. González-Tejera, Kinetic study of poly-N-methylpyrrole electrogeneration, Synth. Met. 142 (2004) 93 – 100

Tables Captions:

Table 1: Energies and selected geometry parameters for hydrolyzed trimer conformers linked α–α' via Py rings, as estimated by *Forcite* coupled with the COMPASS force field analyses.

Figure Captions:

Scheme 1: General synthetic route of N-[ω-(trimethoxysilyl)alkyl]-1H-pyrroles with butyl and hexyl side chains (ω = 4 and 6, Fig. 1a).

Figure 1: Schematic structures of the investigated compounds: (a) pyrrole and N-[ω-(trimethoxysilyl)alkyl]-1H-pyrroles with different alkyl chain lengths (ω = 3, 4 and 6); (b) hydrolyzed α–α' linked N-[ω-(trimethoxysilyl)alkyl]-1H-pyrroles.

Figure 2: FTIR spectra of Hex-5-enyl-1H-pyrrole (top) and N-[6-(trimethoxysilyl)hexyl]-1H pyrrole (bottom) (compounds 2b and 3b in Scheme 1).

Figure 3: Single-cycle potentiodynamic polymerization of (a) pyrrole and (b-d) N-[ω-(trimethoxysilyl)alkyl]-1H-pyrroles (Fig. 1a) using different scan rates and freshly prepared test solutions (4 mM in 0.1M TBAP/CAN). Potential swept from 0.0 V to +2.0 V, then switched to -1.2 V and forwarded to 0.0 V.

Figure 4: Single-cycle voltammograms ($\nu = 100$ mV/s) for pyrrole and N-[ω-(trimethoxysilyl)alkyl]-1H-pyrroles (Fig. 1a) recorded from solutions at 4 mM in 0.1M TBAP/ACN. Potential swept from 0.0 V to + 1.4 V, then switched to -1.2 V and forwarded to 0.0 V.

Figure 5: Cyclic voltammograms ($\nu = 100$ mV/s) for (a) pyrrole and (b-c) N-[ω-(trimethoxysilyl)alkyl]-1H-pyrroles, ω = 3,4,6 respectively (Fig. 1a) recorded from solutions at 4 mM in 0.1M TBAP/ACN. Potential swept from 0.0 V to + 1.4 V (E_A), then switched to -1.2 V and subsequently cycled between -1.2 V and +1.4 V.

Figure 6: Cyclic voltammograms ($\nu = 100$ mV/s) for (a) pyrrole and (b-c) N-[ω-(trimethoxysilyl)alkyl]-1H-pyrroles, ω = 3,4,6 respectively (Fig. 1a) recorded from solutions at 4 mM in 0.1M TBAP/ACN. Potential swept from 0.0 V to + 1.2 V (E_A), then switched to -1.2 V and subsequently cycled between -1.2 V and +1.2 V.

Figure 7: Cyclic voltammograms ($\nu = 100$ mV/s) in monomer-free 0.1M TBAP/MeCN of the electrodeposited films using E_A = +1.2 V (Fig. 6) (a) pyrrole and (b-c) N-[ω-(trimethoxysilyl)alkyl]-

1H-pyrroles, ω = 3,4,6 respectively (Fig. 1a). Potential swept from 0.0 V to + 1.2 V (E_A), then switched to -1.2 V and subsequently cycled between -1.2 V and +1.2 V.

Figure 8: Schematic representation of the most favored bounded hydrolyzed trimer conformations (Table 1): a) 3C2; b) 3C3; c) 4C3; d) 6C3. Solvent molecules (MeOH:H_2O) are not shown.

Table 1

Table 1: Energies and selected geometry parameters for hydrolyzed trimer conformers linked α–α' via Py rings, as estimated by *Forcite* coupled with the COMPASS force field analyses.

Alkyl chain	Trimer conformer	E_{pot}[(a)] kcal/mol	$\Delta E_{interact}$[(b)] kcal/mol	H bond distance[(c)] (Å)	Torsional angle θ_1[(d)] (°)	Torsional angle θ_2[(d)] (°)
Propyl	3C1	-443.9	-86 ± 4	2.0 ± 0.3 (8)	174 ± 6	188 ± 6
(ω = 3)	3C2	-411.0	-172 ± 6	1.9 ± 0.2 (11)	188 ± 6	175 ± 6
	3C3[(e)]	-401.9	-169 ± 6	2.0 ± 0.2 (14)	191 ± 6	184 ± 6
Butyl	4C1	-432.9	-125 ± 6	2.0 ± 0.1 (5)	5.1 ± 6.0	355 ± 7
(ω = 4)	4C2	-450.7	-113 ± 6	2.0 ± 0.2 (8)	173 ± 6	180 ± 6
	4C3[(f)]	-471.1	-222 ± 7	2.0 ± 0.2 (14)	176 ± 6	180 ± 6
Hexyl	6C1	-459.9	-65 ± 5	1.7 ± 0.1 (1)	172 ± 6	12 ± 6
(ω = 6)	6C2	-458.11	-88 ± 9	2.0 ± 0.4 (4)	5.6 ± 6.2	175 ± 6
	6C3	-468.4	-153 ± 7	1.9 ± 0.2 (6)	179 ± 6	189 ± 6

(a)Total energy obtained from the *Forcite* geometry optimization of complexes obtained by *Adsorption Locator* docking module; (b) Interaction energy and the corresponding standard deviations from the post-processing of the *DISCOVER* MD trajectories (eq. 1); (c) number of observed H bonds in parenthesis; (c,d) estimated from the statistical analysis of the average H bond distance and inter-ring torsion angles ∠NCCN distributions (*Forcite* analysis) of the last 500 ps of MD simulation trajectory; additional information on the H-bond distribution are reported in Figures S7-S9, Supporting Information; (d) θ_1 and θ_2 correspond to the inter-ring torsion angles ∠NCCN between the adjacent α-α' linked pyrroles, estimated from the statistical analysis of the torsion distributions (*Forcite* analysis) of the last 500 ps of MD simulation trajectory; (e) estimated for the last 500 ns of a 1.5 ns trajectory; (f) estimated for the last 500 ns of a 2.0 ns trajectory.

Scheme 1

Click here to download high resolution image

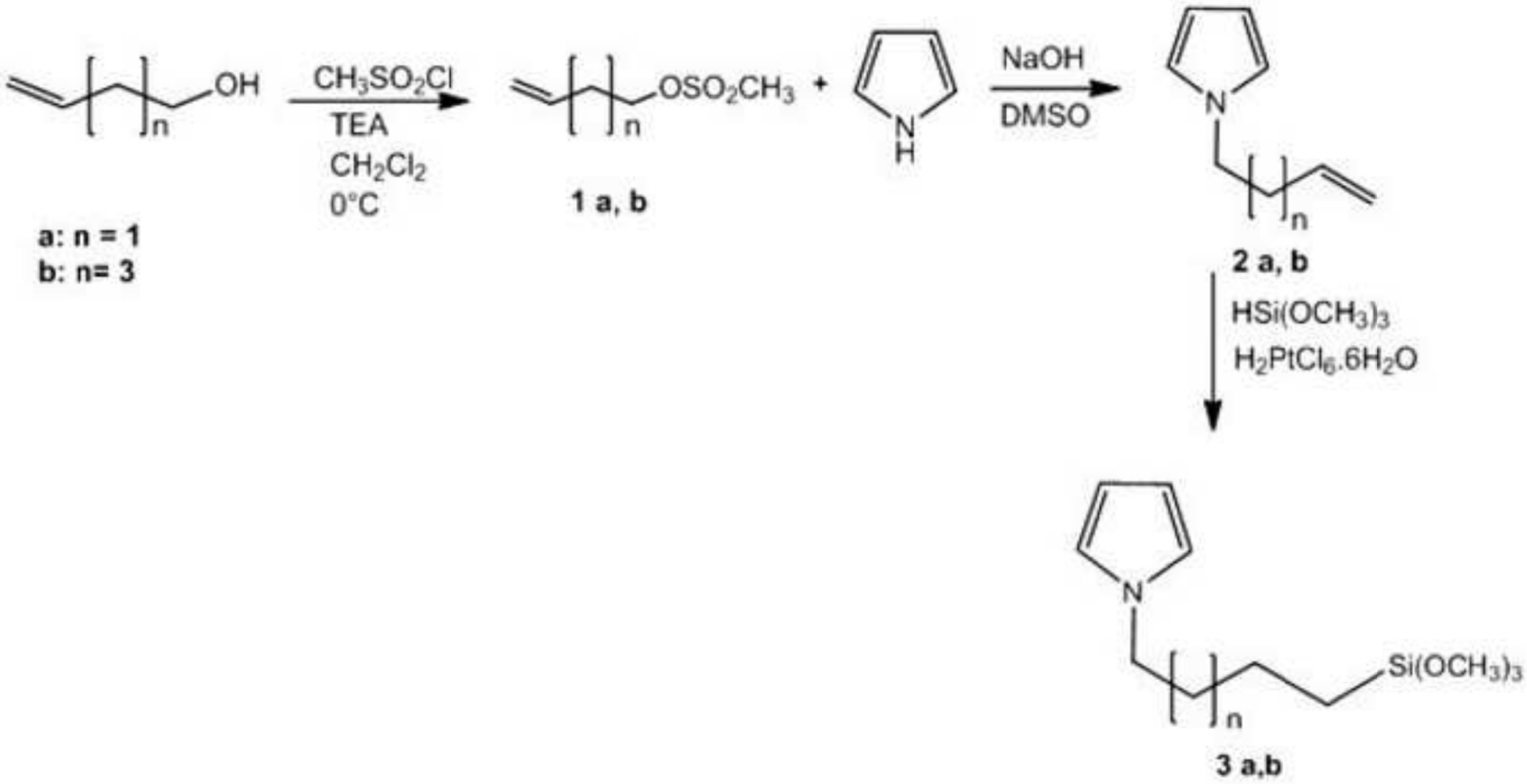

a: n = 1
b: n= 3

Figure 1
Click here to download high resolution image

(a)

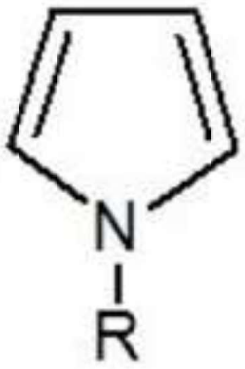

$R = - (CH_2)_\omega - Si - (OCH_3)_3$

$(\omega = 3,4,6)$

(b)

$R = - (CH_2)_\omega - Si - (OH)_3$

$(\omega = 3,4,6)$

Figure 2

Click here to download high resolution image

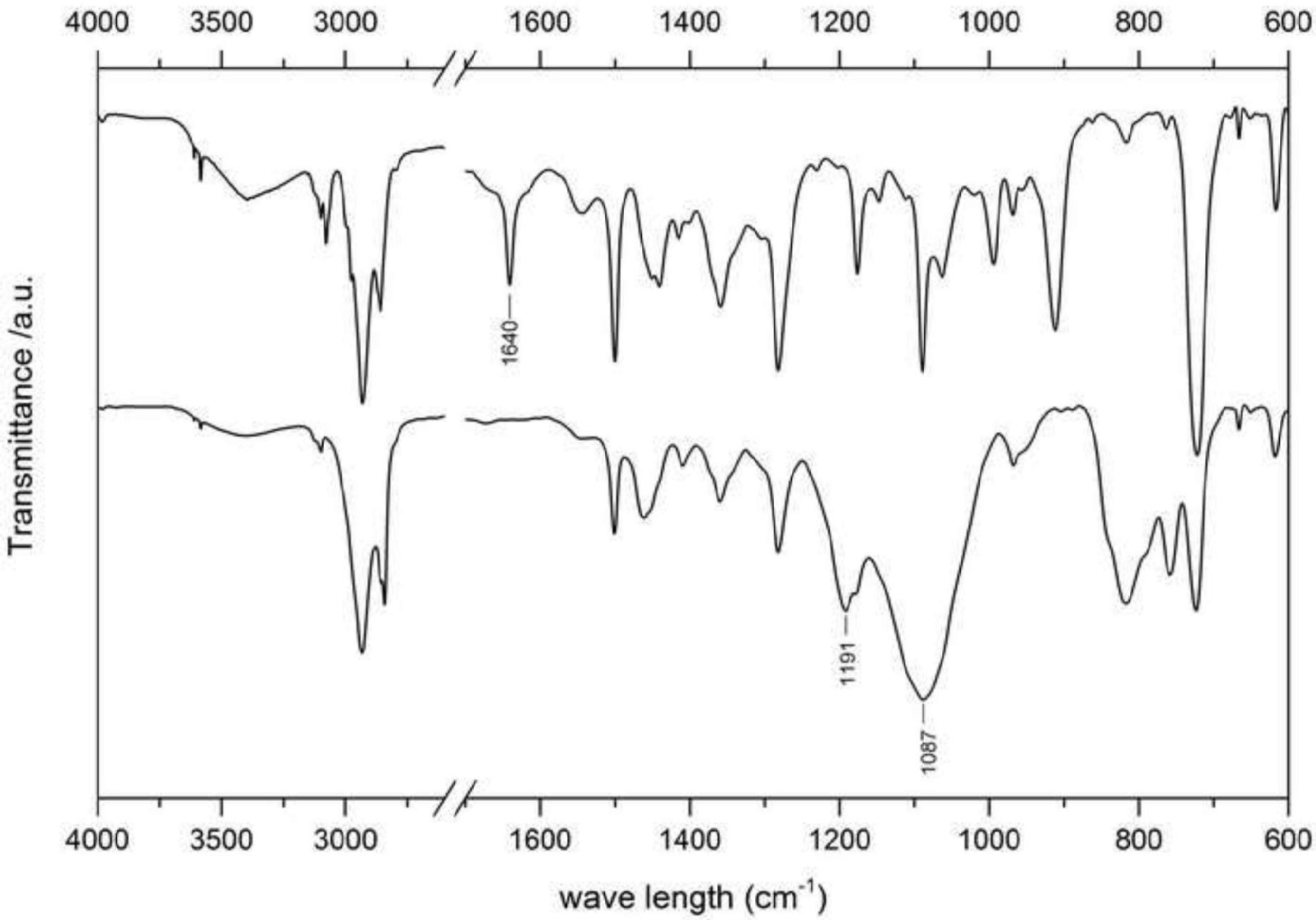

Figure 3

Click here to download high resolution image

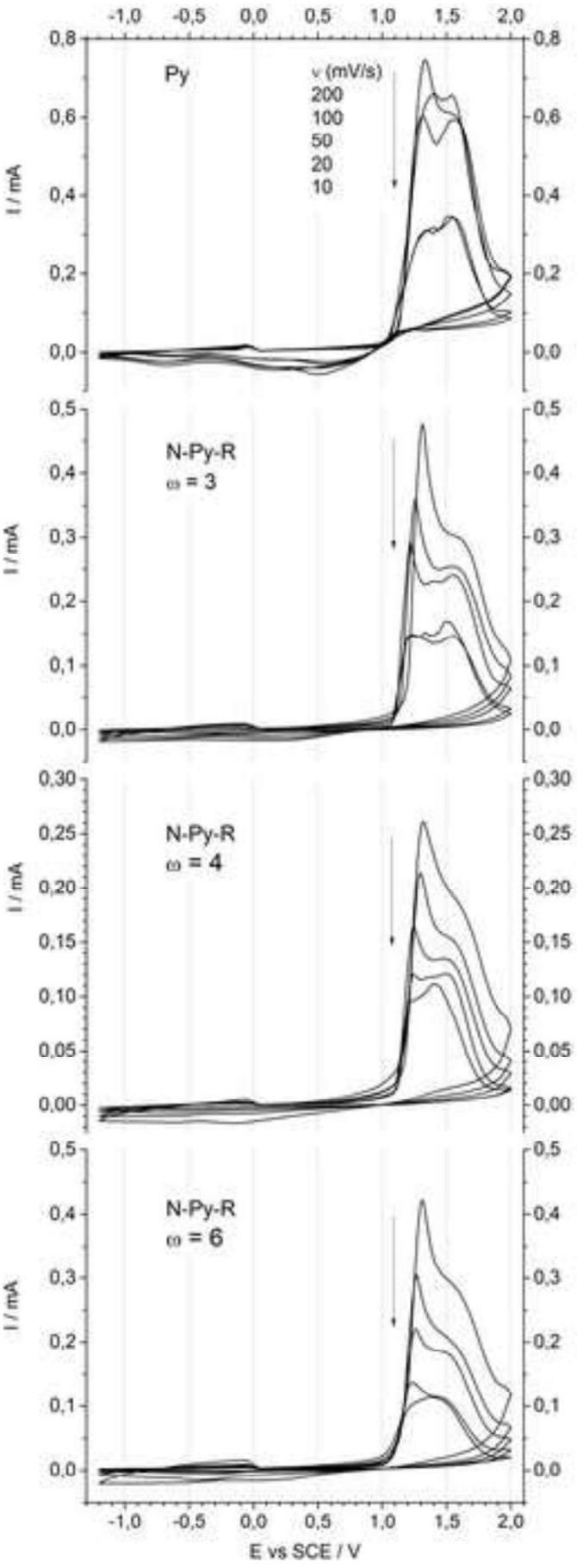

Figure 4

Click here to download high resolution image

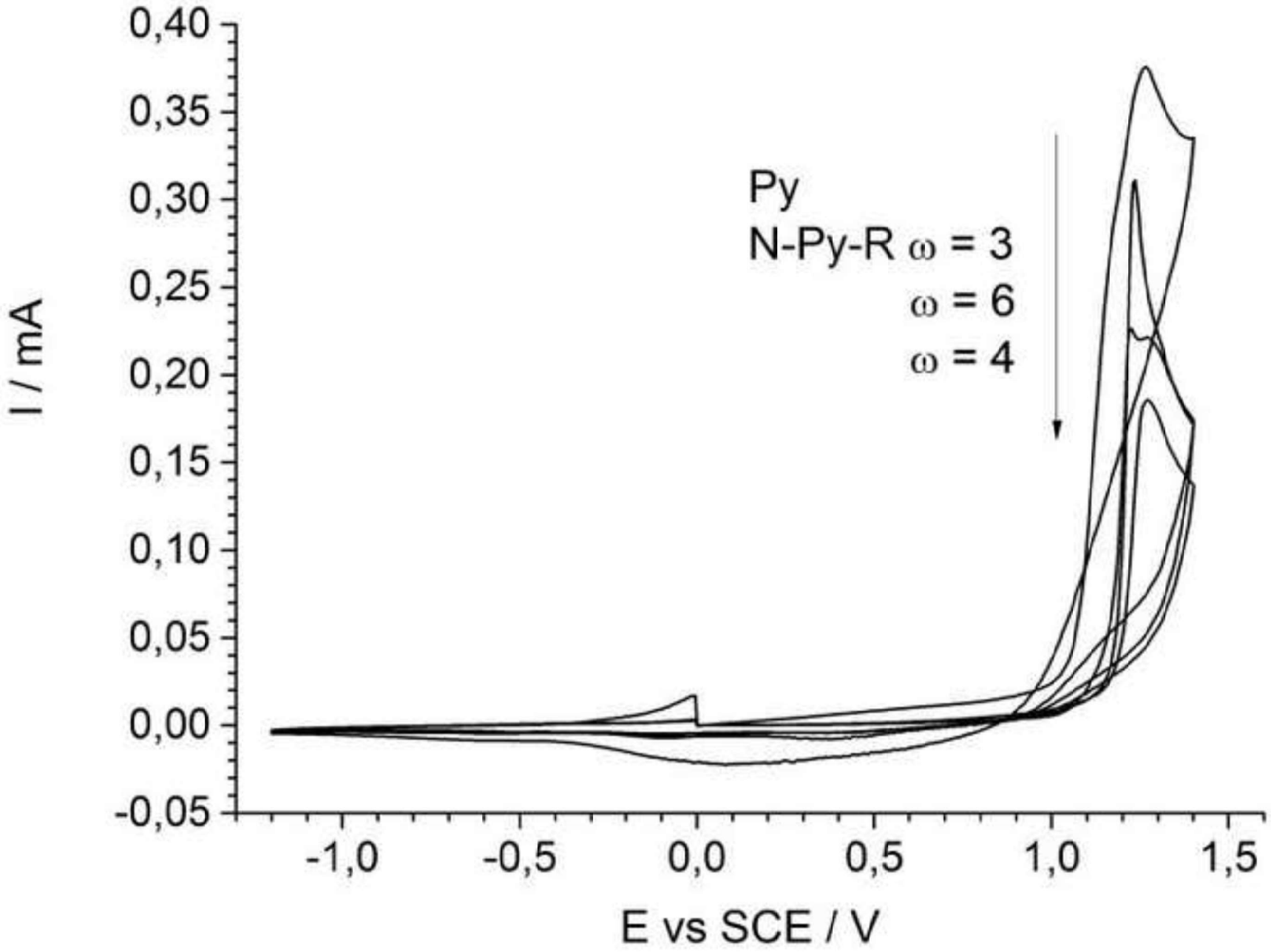

Figure 5
Click here to download high resolution image

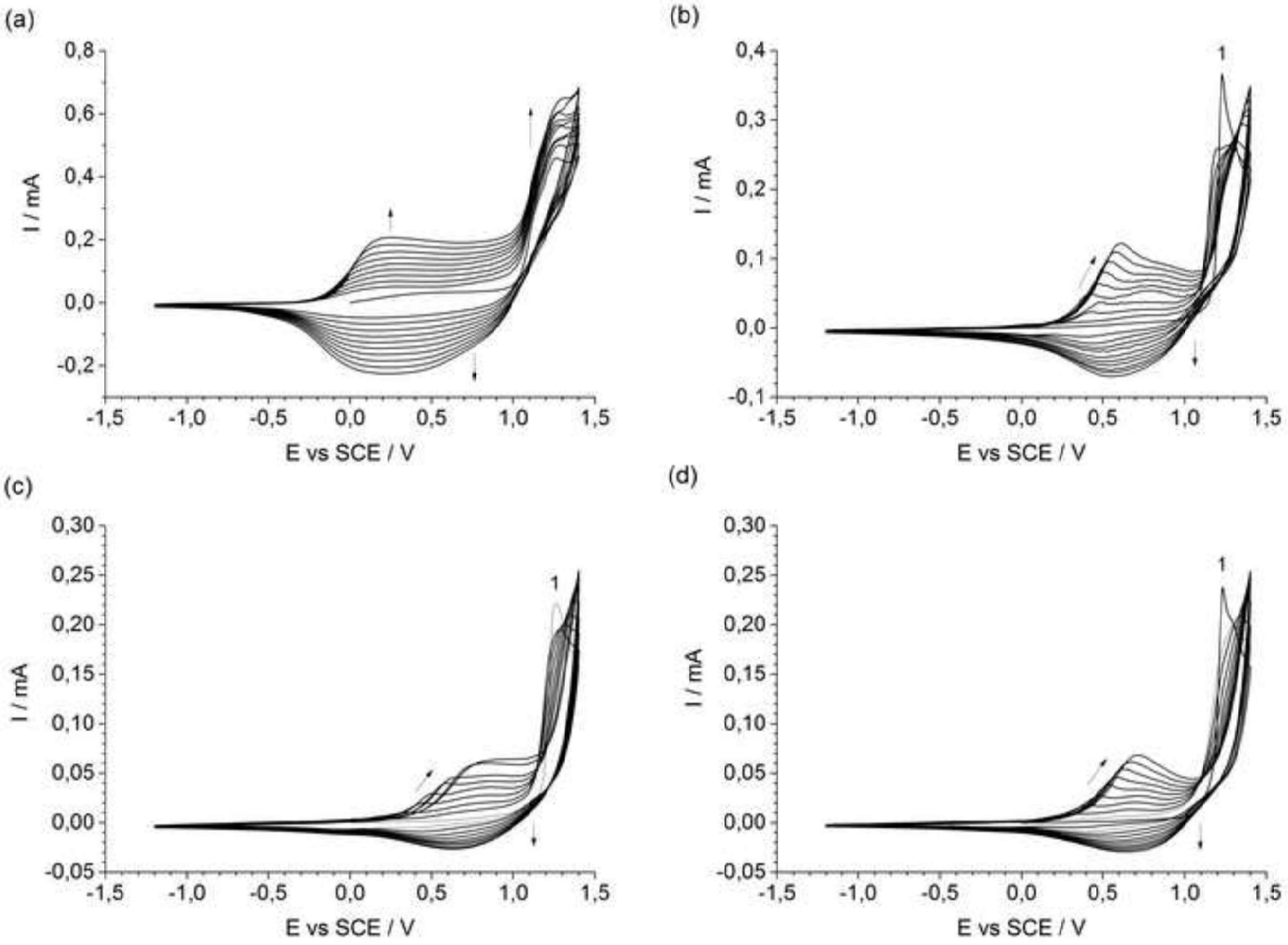

Figure 6

Click here to download high resolution image

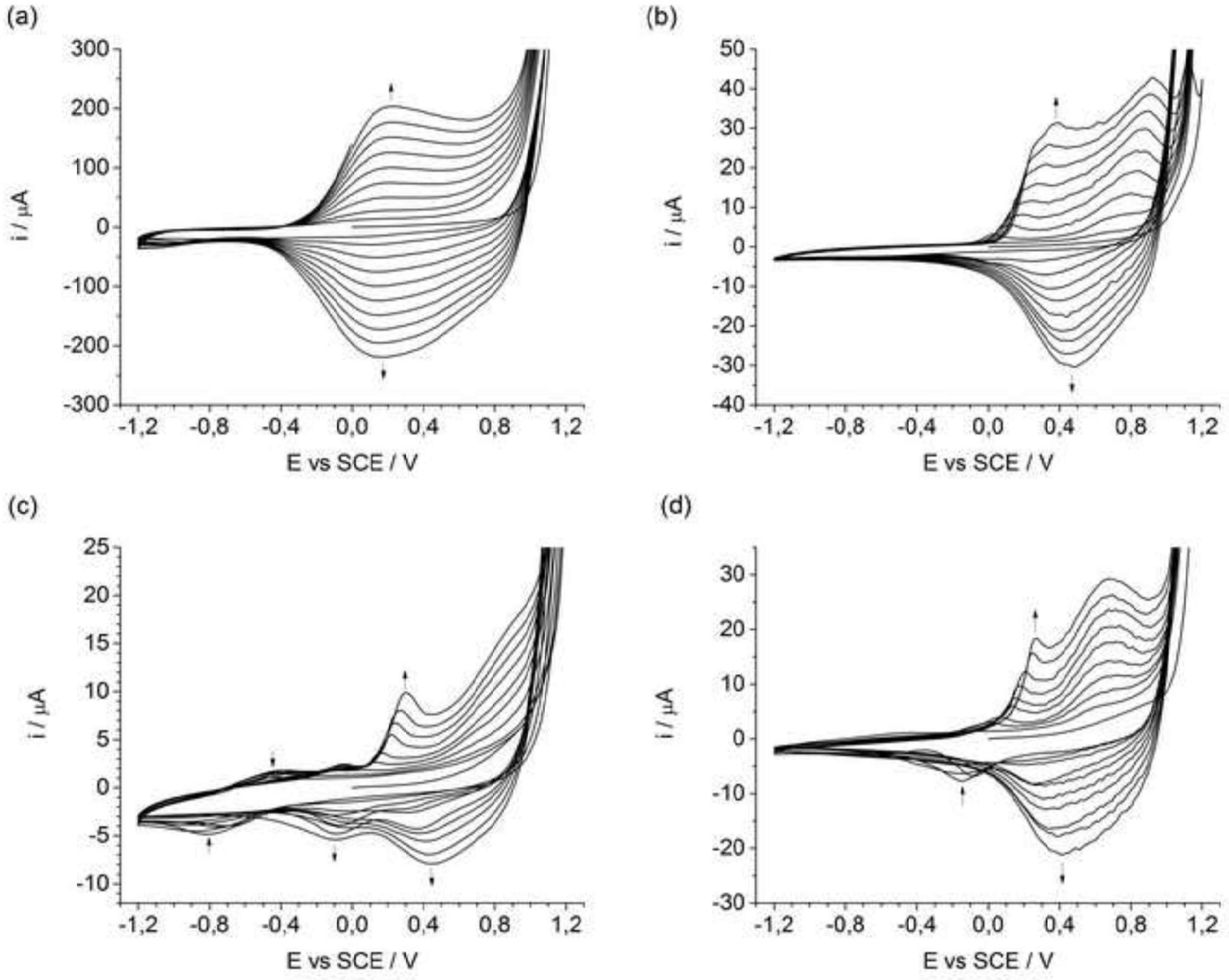

Figure 7
Click here to download high resolution image

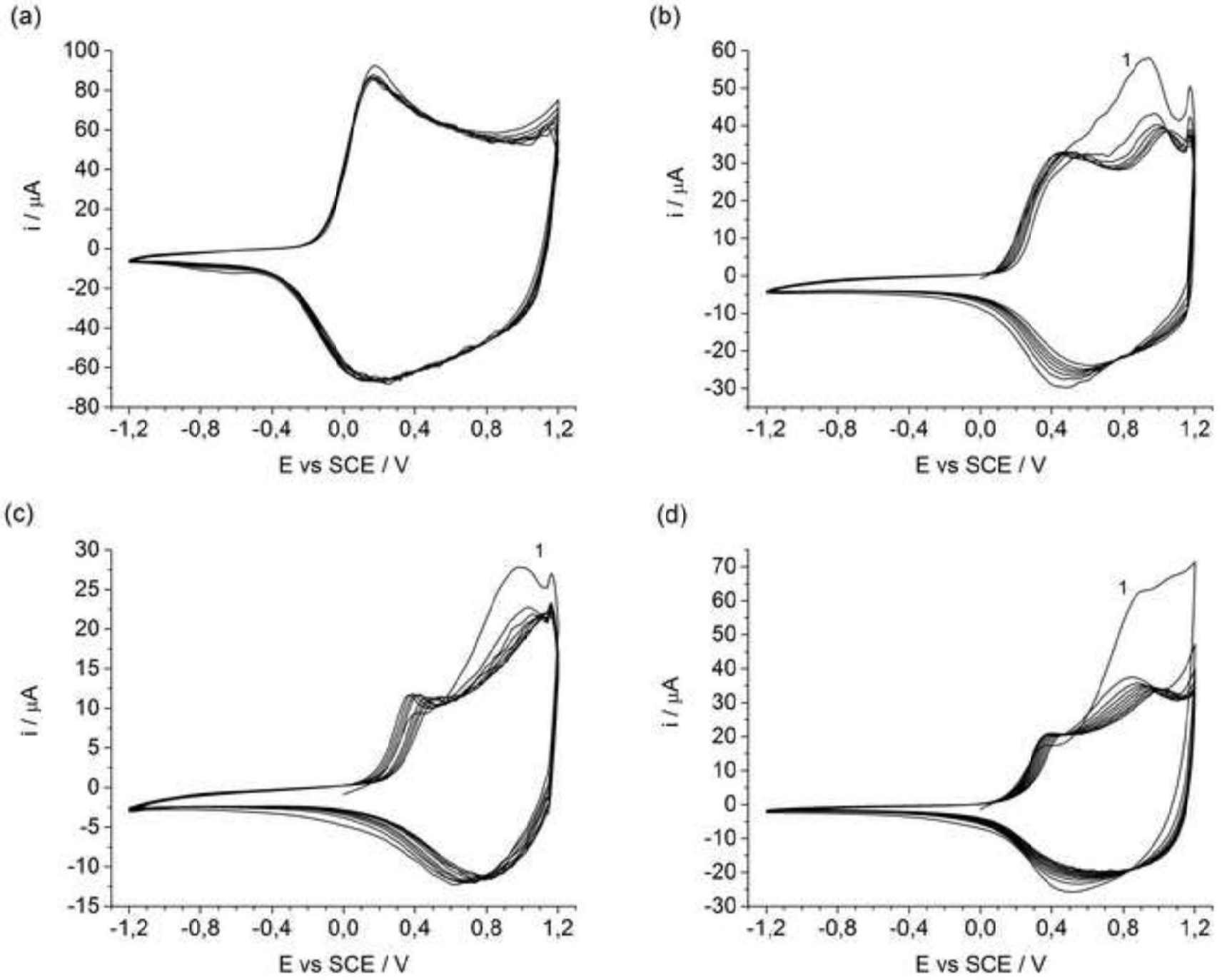

Figure 8
Click here to download high resolution image

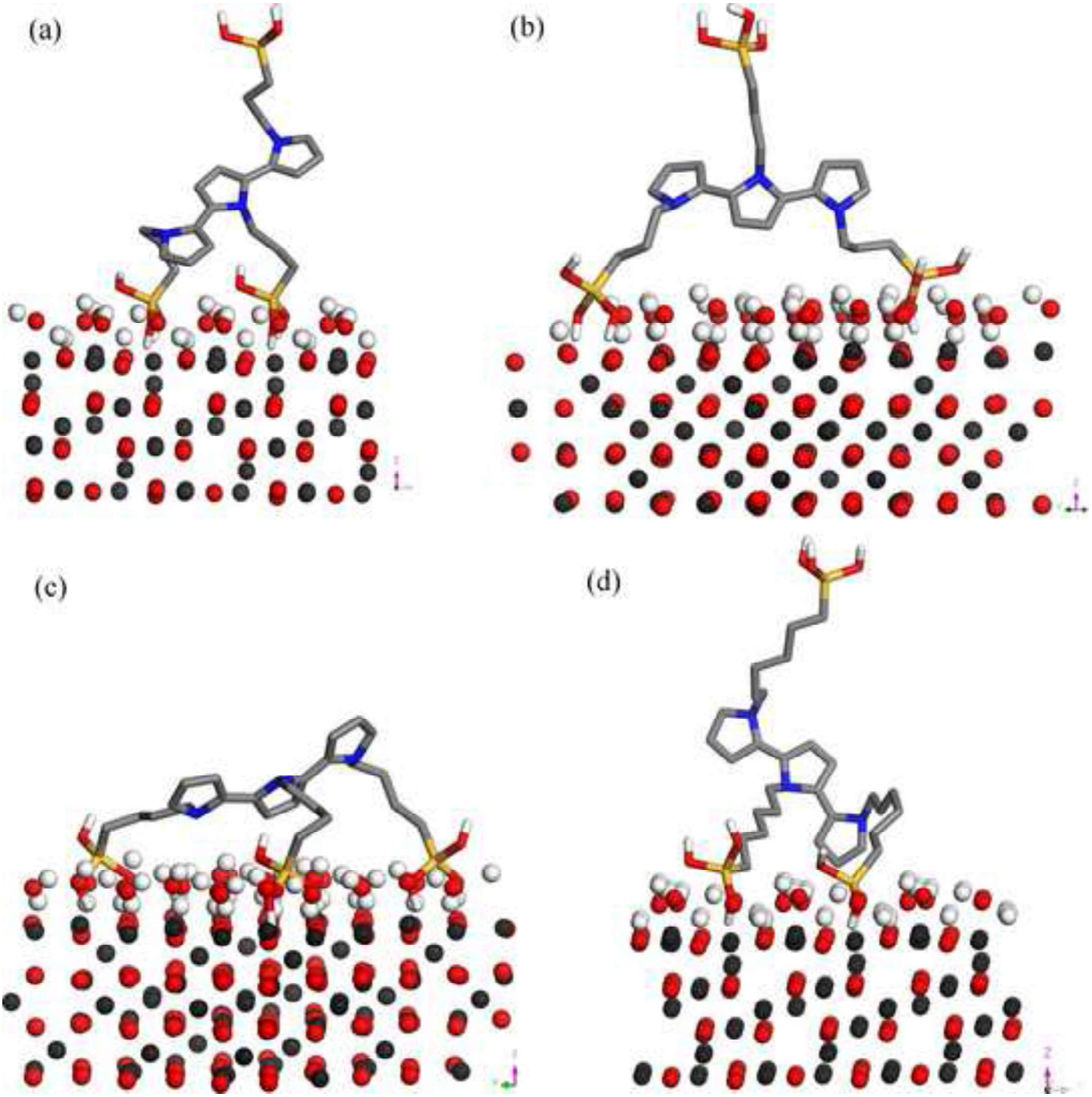

Pyrrolyl-silicon compounds with different alkyl spacer lengths: synthesis, electrochemical behavior and binding properties.

E. Volpi[a], L. Falciola[a], M. Trueba[a*], S.P. Trasatti[a], M.C. Sala[b], E. Pini[b], A. Contini[b]

[a]Dipartimento di Chimica, Università degli Studi di Milano, Via Golgi 19, 20133 , Milano, Italy

[b]Dipartimento di Scienze Farmaceutiche-Sezione Chimica Generale e Organica "A. Marchesini", Università degli Studi di Milano, Via Venezian 21, 20133 , Milano, Italy

*Corresponding author: monica.trueba@unimi.it

Supporting Information

Table S1: NMR (^{1}H, ^{13}C), MS, and FTIR characterization data of intermediate and final products of the synthetic route in Scheme 1.

Figure S1: Cyclic voltammograms (ν = 100 mV/s) in monomer-free 0.1M TBAP/MeCN of the electrodeposited films using E_A = +1.4 V (Fig. 5): (a) pyrrole and (b-c) N-[ω-(trimethoxysilyl)alkyl]-1H-pyrroles, ω = 3,4,6 respectively (Fig. 1a). Potential swept from 0.0 V to + 1.4 V (E_A), then switched to -1.2 V and subsequently cycled between -1.2 V and +1.4 V.

Figure S2: N-[3-(trihydroxysilyl)propyl]-1H-pyrrole - Interaction energies and H-bond distributions of α–α' Py linked trimer conformers 3-C1 (8 HBs), 3-C2 (11 HBs) and 3-C3 (14 HBs).

Figure S3: N-[4-(trihydroxysilyl)butyl]-1H-pyrrole - Interaction energies and H-bond distribution of α–α' Py linked trimer conformers 4-C1 (5 HBs), 4-C2 (8 HBs) and 4-C3 (14 HBs).

Figure S4: N-[6-(trihydroxysilyl)hexyl]-1H-pyrrole - Interaction energies and H-bond distributions of α–α' Py linked trimer conformers 6-C1 (1 HB), 6-C2 (4 HBs) and 6-C3 (6 HBs)

Figure S5: Binding conformation 3C1 of α–α'Py-$(CH_2)_\omega$-$Si(OH)_3$ trimer structures with propyl side chain (ω = 3). Al atoms are represented in dark gray.

Figure S6: H-bond details for the binding conformation 3C1 (Fig. S5)

Figure S7: Binding conformations 4C1 and 4C2 for α–α'Py-$(CH_2)_\omega$-$Si(OH)_3$ trimer structures with butyl side chain (ω = 4). Al atoms are represented in dark gray.

Figure S8: Binding conformations 6C1 and 6C2 for α–α'Py-$(CH_2)_\omega$-$Si(OH)_3$ trimer structures with hexyl side chain (ω = 6). Al atoms are represented in dark gray.

Table S1: NMR (^{1}H, ^{13}C), MS, and FTIR data of intermediate and final products of the synthetic route in Scheme 1.

But-3-en-1-methanesulfonate (1a): yield 99 %
^{1}H NMR (200 MHz, $CDCl_3$): δ = 5.79 (1H, ddt, J= 6.6, J= 10.2, J= 17.0Hz , =CH), 5.22-5.11 (m, 2H, $=CH_2$), 4.25 (t, J= 6.6 Hz, 2H, CH_2O), 2.99 (s, 3H, CH_3), 2.50 (m, 2H, $=CHCH_2$) ppm. ^{13}C NMR (50.3 MHz, $CDCl_3$): δ132.6, 118.7, 69.0, 37.7, 33.6 C_3 ppm. IR (NaCl): ν_{max} 3082 (ν C sp^2-H), 3023, 2984, 2942 (ν C sp^3-H), 1643 (ν C=C), 1352 (ν_{asim}O=S=O),1174 (ν_{sim} O=S=O) cm^{-1}. $[M+H]^+$ 150 m/z.

Hex-5-en-1-methanesulfonate (1b): yield 99 %
^{1}H NMR (200 MHz, $CDCl_3$): δ = 5.77 (ddt, J= 6.6, J= 10.3, J= 14.6 Hz , 1H, =CH), 5.07-4.99 (m, 2H, $=CH_2$),4.23 (t, J= 6.3 Hz , 2H, CH_2O), 2.99 (s, 3H, CH_3), 2.09 (m, 2H, $=CHCH_2$), 1.82-1.65 (m, 2H, CH_2), 1.57-1.45 (m, 2H, CH_2) ppm. ^{13}C NMR (50.3 MHz, $CDCl_3$): δ 138.1, 115.4 C_1, 70.2, 37.5, 33.2, 28.7, 24.8 ppm. IR (NaCl): ν_{max} 3078 (ν C sp^2-H), 2976, 2941, 2862 (ν C sp^3-H), 1641 (ν C=C), 1353 (ν_{asim}O=S=O), 1174 (ν_{sim} O=S=O)) cm^{-1}.$[M+H]^+$ 179m/z.

But-3-enyl-1H-pyrrole (2a): yield 68 %
^{1}H NMR (200 MHz, $CDCl_3$): δ = 6.67 (t, J= 2.2, 2H, =CHN),6.15 (t, J= 2.2Hz, 2H, =CH), 5.77 (ddt, J= 6.6, J= 10.8, J= 16.6Hz , 1H, CH_2=CH), 5.13-5.04 (m, 2H, $=CH_2$), 3.95 (t, J= 7.0Hz , 2H,CH_2N), 2.52 (dquart, J= 7.0, J= 1.3 Hz, 2H, CH_2CH_2N) ppm.^{13}C NMR (50.3 MHz, $CDCl_3$): δ 134.8, 120.7, 117.4, 108.2, 49.4, 36.1 ppm. IR (NaCl): ν_{max} 3100, 3079 (ν C sp^2-H), 2927, 2855 (ν C sp^3-H), 1640 (ν C=C),1500-1283 (aromatic vibrations of pyrrolic ring), 1089-622 (bending pyrrolic ring) cm^{-1}. $[M+H]^+$ 122 m/z.

Hex-5-enyl-1H-pyrrole (2b): yield 66%
^{1}H NMR (200 MHz, $CDCl_3$): δ 6.66 (t, J= 2.2 Hz , 2H, =CHN), 6.15 (t, J= 2.2 Hz , 2H, CH=CH), 5.77 (ddt, J= 6.6, J= 10.0, J = 16.9 Hz , 1H, CH_2=CH), 5.07-4.99 (m, 2H, $=CH_2$), 3.88 (t, J= 7.0 Hz , 2H, CH_2N), 2.03 (dquart, J= 8.0, J= 1.1 Hz, 2H, CH_2), 1.86-1.71 (m, 2H, CH_2); 1.47-1.32 (m, 2H, CH_2) ppm. ^{13}C NMR (50.3 MHz, $CDCl_3$): δ 138.5, 120.7, 115.1, 108.0, 49.7, 33.5, 31.2, 26.2 ppm. . IR (NaCl): ν_{max} 3099, 3076 (ν C sp^2-H), 2931,2851 (ν C sp^3-H), 1640 (ν C=C), 1500-1358 (vibrations pyrrolic ring), 1280-600 (bending pyrrolic ring) cm^{-1}.$[M+H]^+$ 150 m/z.

N-[4-(trimethoxysilyl)butyl]-1H-pyrrole (3a): yield 43%
^{1}H NMR (200 MHz, $CDCl_3$): δ6.66 (t, J= 2.2 Hz, 2H, =CHN), 6.13 (t, J= 2.2 Hz, 2H, =CH), 3.86 (t, J= 7.3 Hz, 2H, CH_2N), 3.67 (s, 9H, OCH_3), 1.82 (quint, J= 7.3 Hz, 2H, CH_2), 1.49-1.35 (m, 2H, CH_2), 0.70-0.62 (m, 2H, CH_2-Si) ppm.^{13}C NMR (50.3 MHz, $CDCl_3$):δ 120.7, 108.0, 50.7, 49.4, 34.84, 20.2, 9.0 ppm. IR (NaCl): ν_{max} 3100 (ν C sp^2-H), 2942-2841 (ν C sp^3-H), 1594-1282 (vibrations pyrrolic ring), 1191 (ν Si-O-CH_3), 1087 (ν Si-O) cm^{-1}. $[M+H]^+$244 m/z.

N-[6-(trimethoxysilyl)hexyl]-1H-pyrrole(3b): yield 92%
^{1}H NMR (200 MHz, $CDCl_3$): δ 6.64 (t, J= 2.2 Hz, 2H, =CHN), 6.13 (t, J= 2.2 Hz, 2H, =CH), 3.86 (t, J= 7.4 Hz, 2H, CH_2N), 3.56 (s, 9H, OCH_3), 1.75 (quint, J= 7.4 Hz, 2H, CH_2), 1.42-1.20 (m, 6H, CH_2), 0.67-0.59 (m, 2H, CH_2-Si) ppm.^{13}C NMR (50.3 MHz, $CDCl_3$):δ 120.6, 108.0, 50.7, 49.8, 32.8, 31.6, 26.6, 22.7, 9.3 ppm. IR (NaCl): 3100 (ν C sp^2-H), 2933; 2841 (ν C sp^3-H), 1500-1281 (vibrations pyrrolic ring), 1191 (ν Si-O-CH_3), 1088 (ν Si-O) cm^{-1}. $[M+H]^+$272 m/z.

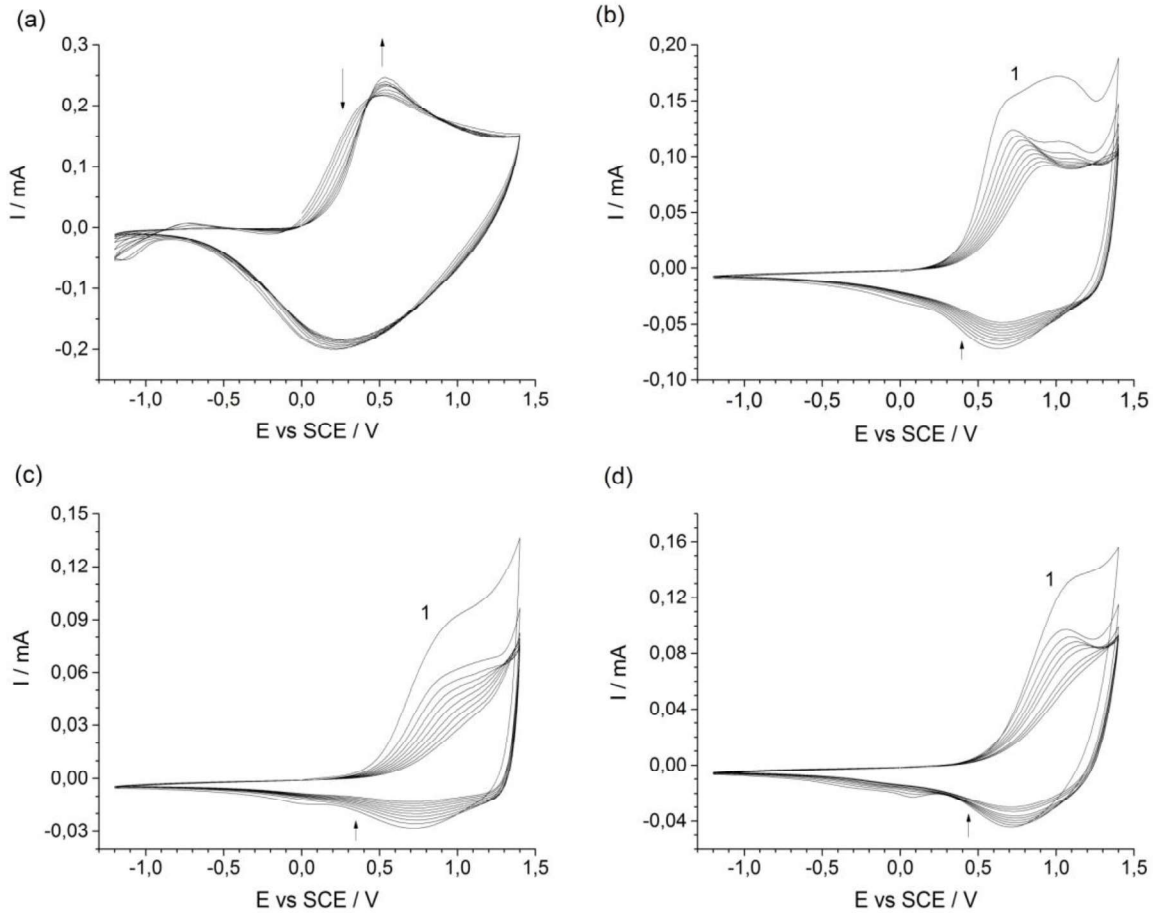

Figure S1: Cyclic voltammograms (ν = 100 mV s^{-1}) in monomer-free 0.1M TBAP/MeCN of the electrodeposited films using E_A = +1.4 V (Fig. 5): (a) pyrrole and (b-c) N-[ω-(trimethoxysilyl)alkyl]-1H-pyrroles, ω = 3,4,6 respectively (Fig. 1a). Potential swept from 0.0 V to + 1.4 V (E_A), then switched to -1.2 V and subsequently cycled between -1.2 V and +1.4 V.

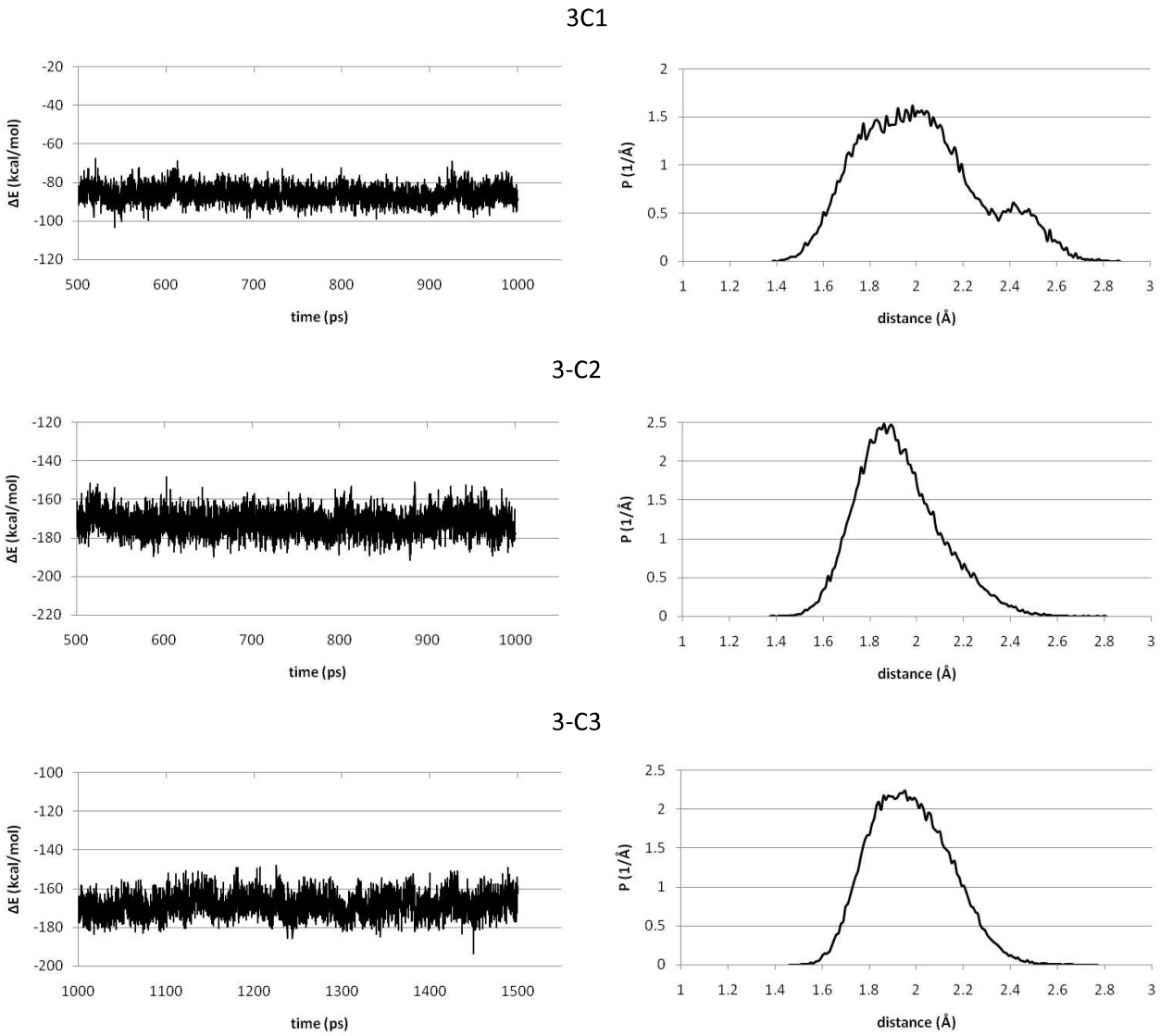

Figure S2: N-[3-(trihydroxysilyl)propyl]-1H-pyrrole - Interaction energies and H-bond distributions of α–α' Py linked trimer conformers 3-C1 (8 HBs), 3-C2 (11 HBs) and 3-C3 (14 HBs)

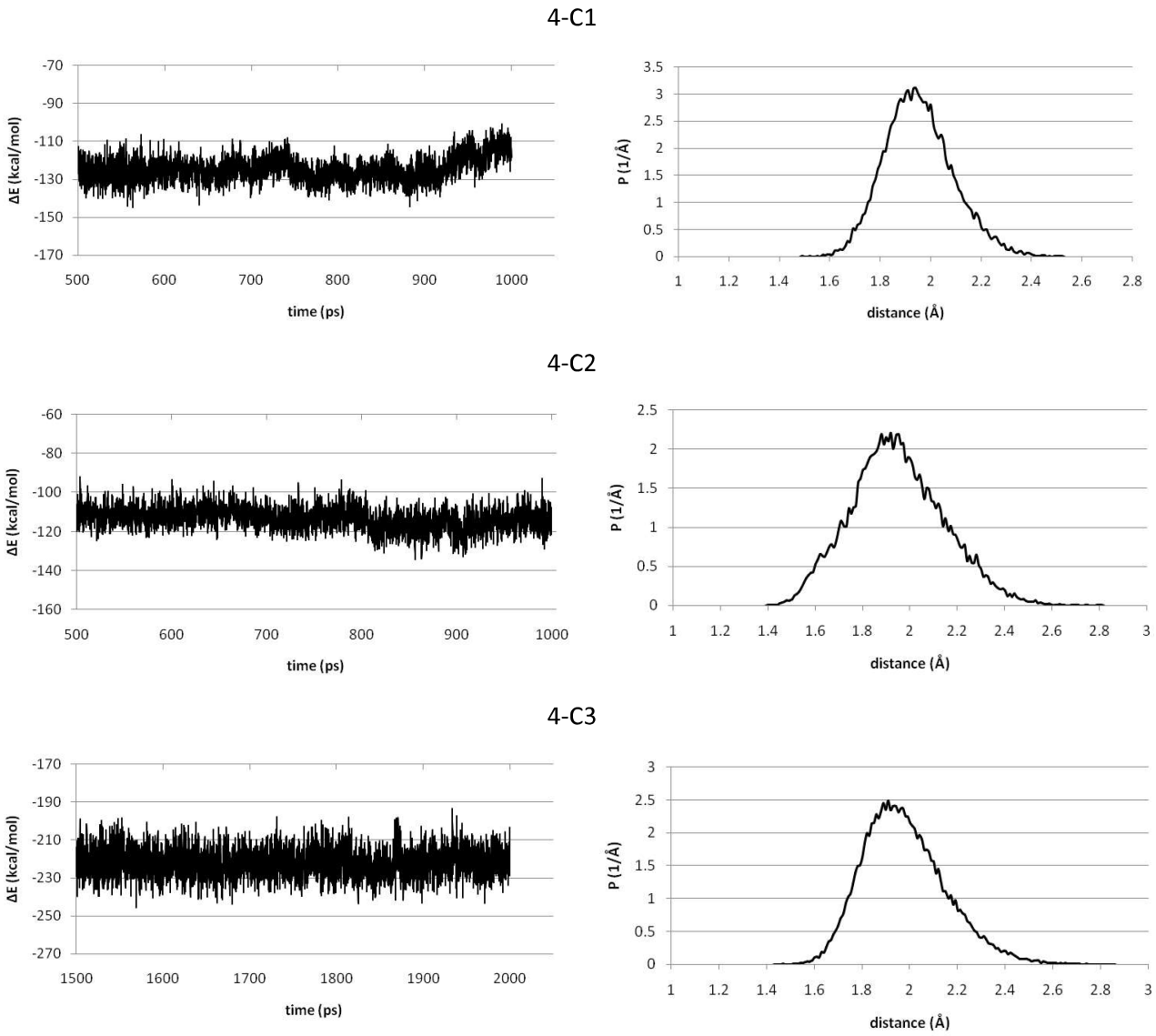

Figure S3: N-[4-(trihydroxysilyl)butyl]-1H-pyrrole - Interaction energies and H-bond distribution of α–α' Py linked trimer conformers 4-C1 (5 HBs), 4-C2 (8 HBs) and 4-C3 (14 HBs)

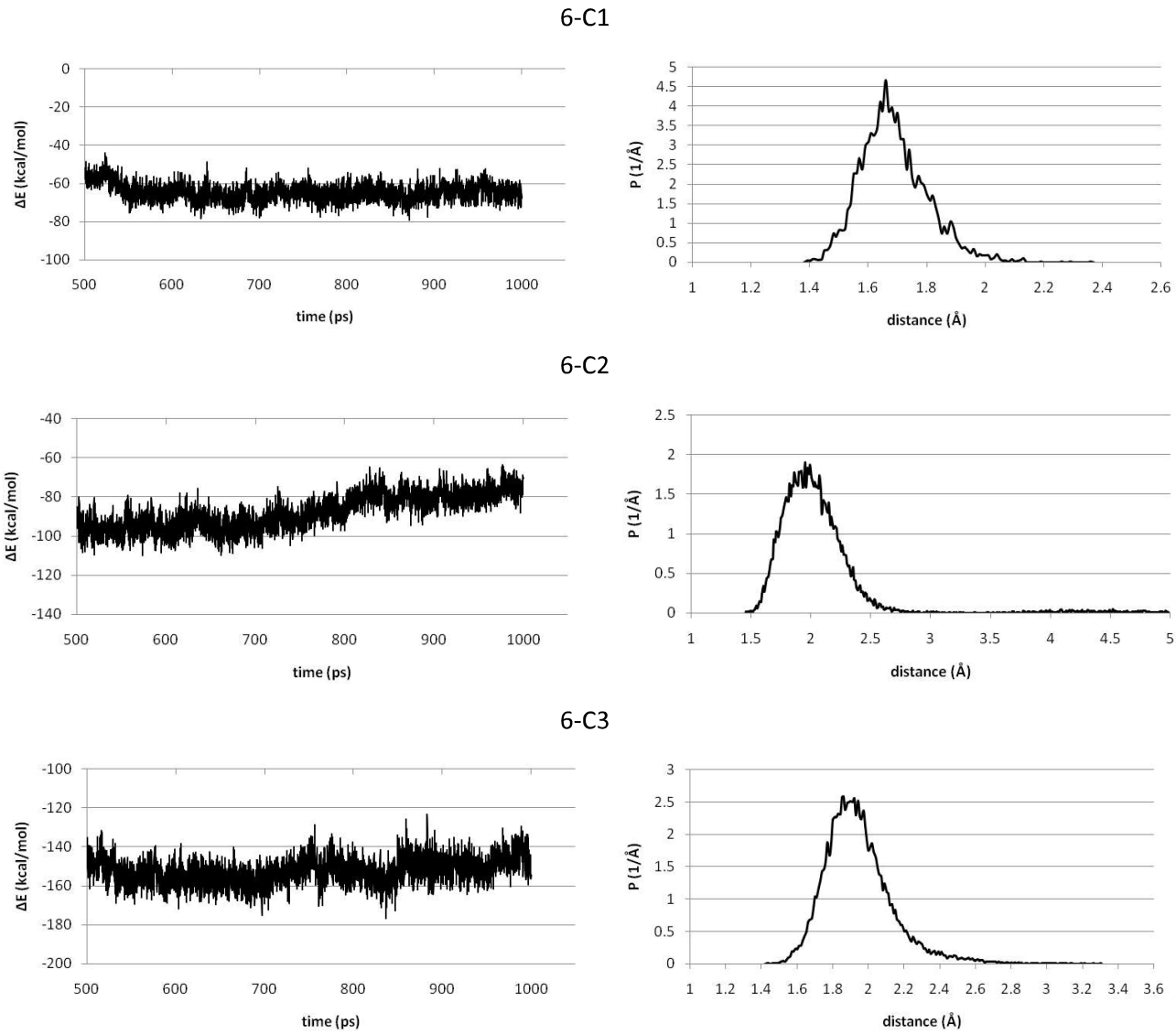

Figure S4: N-[6-(trihydroxysilyl)hexyl]-1H-pyrrole - Interaction energies and H-bond distributions of α–α' Py linked trimer conformers 6-C1 (1 HB), 6-C2 (4 HBs) and 6-C3 (6 HBs)

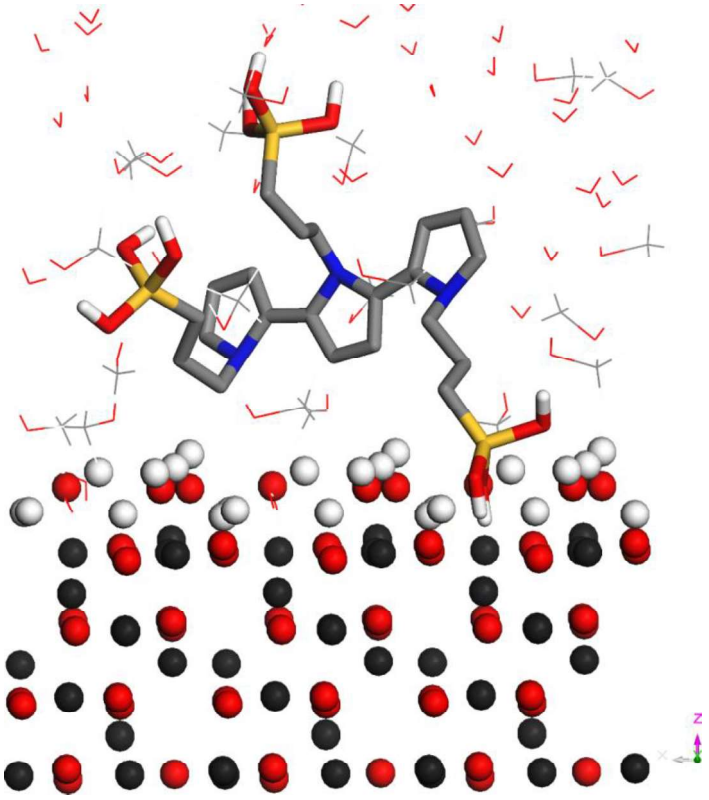

Figure S5: Binding conformation 3C1 of α–α'Py-$(CH_2)_\omega$-$Si(OH)_3$ trimer structures with propyl side chain (ω = 3). Al atoms are represented in dark gray.

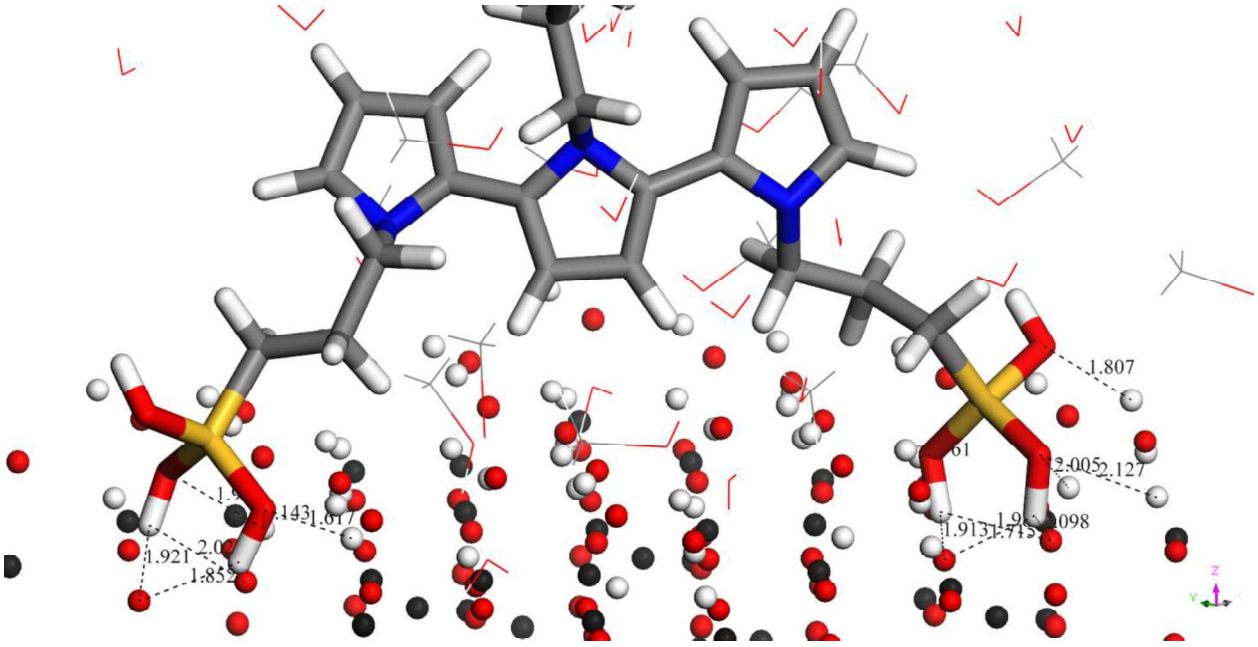

Figure S6: H-bond details for the binding conformation 3C1 (Fig. S5)

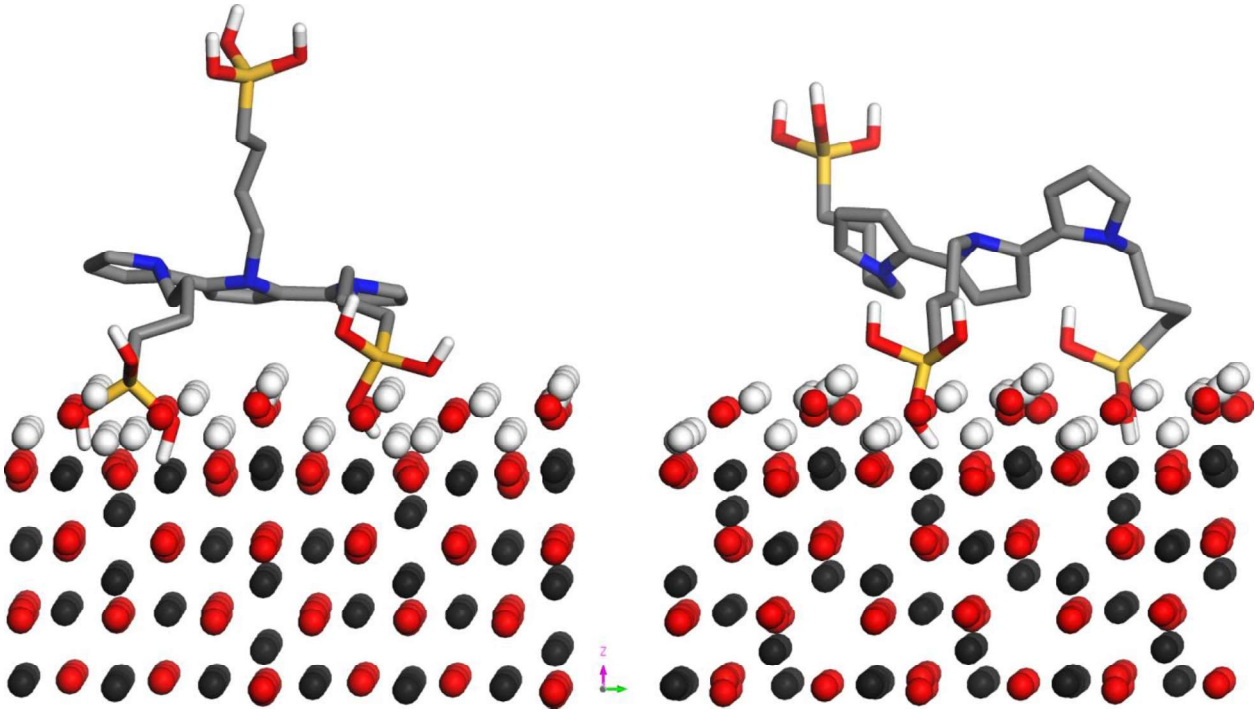

Figure S7: Binding conformations 4C1 and 4C2 for α–α'Py-$(CH_2)_\omega$-$Si(OH)_3$ trimer structures with butyl side chain (ω = 4). Al atoms are represented in dark gray.

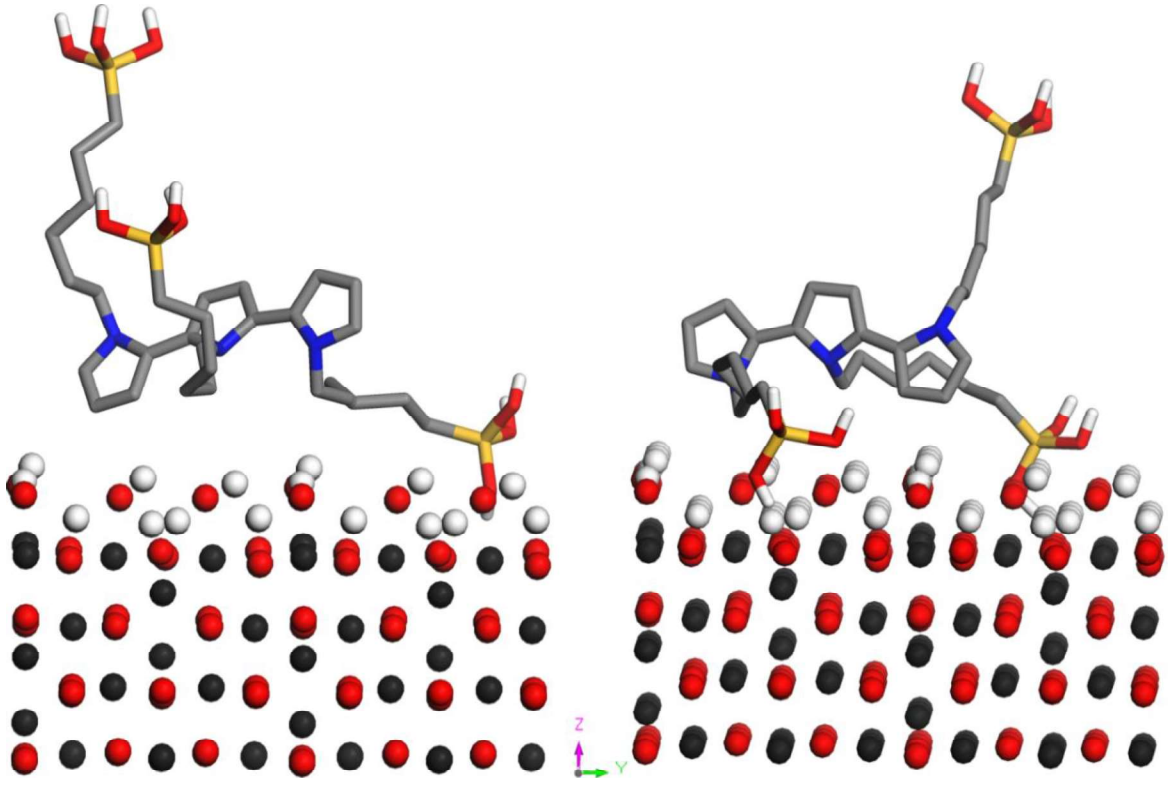

Figure S8: Binding conformations 6C1 and 6C2 for α–α'Py-$(CH_2)_\omega$-$Si(OH)_3$ trimer structures with hexyl side chain (ω = 6). Al atoms are represented in dark gray.